

# 1 **Structure and evolution of the lunar Procellarum region as revealed** 2 **by GRAIL gravity data**

3 Jeffrey C. Andrews-Hanna<sup>1\*</sup>, Jonathan Besserer<sup>2</sup>, James W. Head III<sup>3</sup>, Carly J. A. Howett<sup>4</sup>,  
4 Walter S. Kiefer<sup>5</sup>, Paul J. Lucey<sup>6</sup>, Patrick J. McGovern<sup>5</sup>, H. Jay Melosh<sup>7</sup>, Gregory A. Neumann<sup>8</sup>,  
5 Roger J. Phillips<sup>4</sup>, Paul M. Schenk<sup>5</sup>, David E. Smith<sup>9</sup>, Sean C. Solomon<sup>10,11</sup> and Maria T. Zuber<sup>9</sup>

6 *<sup>1</sup>Department of Geophysics and Center for Space Resources, Colorado School of Mines, Golden,*  
7 *CO 80401, USA. <sup>2</sup>Department of Earth and Planetary Sciences, University of California, Santa*  
8 *Cruz, CA 95064, USA. <sup>3</sup>Department of Geological Sciences, Brown University, Providence, RI*  
9 *02912, USA. <sup>4</sup>Planetary Science Directorate, Southwest Research Institute, Boulder, CO 80302,*  
10 *USA. <sup>5</sup>Lunar and Planetary Institute, Houston, TX 77058, USA. <sup>6</sup>Hawaii Institute of Geophysics*  
11 *and Planetology, University of Hawaii, Honolulu, HI 96822, USA. <sup>7</sup>Department of Earth,*  
12 *Atmospheric, and Planetary Sciences, Purdue University, West Lafayette, IN 47907, USA. <sup>8</sup>Solar*  
13 *System Exploration Division, NASA Goddard Space Flight Center, Greenbelt, MD 20771, USA.*  
14 *<sup>9</sup>Department of Earth, Atmospheric and Planetary Sciences, Massachusetts Institute of*  
15 *Technology, Cambridge, MA 02139-4307, USA. <sup>10</sup>Department of Terrestrial Magnetism,*  
16 *Carnegie Institution of Washington, Washington, DC 20015, USA. <sup>11</sup>Lamont-Doherty Earth*  
17 *Observatory, Columbia University, Palisades, NY 10964 USA.*

18

19 **The Procellarum region is a broad area on the nearside of the Moon that is characterized**  
20 **by low elevations<sup>1</sup>, thin crust<sup>2</sup>, and high surface concentrations of the heat-producing**  
21 **elements uranium, thorium, and potassium<sup>3,4</sup>. The Procellarum region has been interpreted**

22 as an ancient impact basin approximately 3200 km in diameter<sup>5-7</sup>, though supporting  
23 evidence at the surface would have been largely obscured as a result of the great antiquity  
24 and poor preservation of any diagnostic features. Here we use data from the Gravity  
25 Recovery and Interior Laboratory (GRAIL) mission<sup>8</sup> to examine the subsurface structure  
26 of Procellarum. The Bouguer gravity anomalies and gravity gradients reveal a pattern of  
27 narrow linear anomalies that border the Procellarum region and are interpreted to be the  
28 frozen remnants of lava-filled rifts and the underlying feeder dikes that served as the  
29 magma plumbing system for much of the nearside mare volcanism. The discontinuous  
30 surface structures that were earlier interpreted as remnants of an impact basin rim are  
31 shown in GRAIL data to be a part of this continuous set of quasi-rectangular border  
32 structures with angular intersections, contrary to the expected circular or elliptical shape  
33 of an impact basin<sup>9</sup>. The spatial pattern of magmatic-tectonic structures bounding  
34 Procellarum is consistent with their formation in response to thermal stresses produced by  
35 the differential cooling of the province relative to its surroundings, coupled with magmatic  
36 activity driven by the elevated heat flux in the region.

37

38 The Procellarum KREEP Terrane (PKT) is defined by higher than average values of the  
39 surface abundances of potassium, rare earth elements, and phosphorus<sup>3,10</sup> (Fig. 1). The PKT  
40 likely experienced a geodynamical history that differed from that of the rest of the Moon because  
41 of the elevated heat flow resulting from the high crustal concentrations of heat-producing  
42 elements<sup>10-12</sup>. The region encompasses the majority of the mare basalt provinces, including many  
43 that are not associated with known impact basins. The interpretation of the region as an impact  
44 basin was based on its distinctive composition and generally low elevation, together with the

45 photogeological interpretation of features as fragments of circular basin rings<sup>5-7,13</sup>. The most  
46 prominent candidate ring structures are the mare shorelines and scarps on the western edge of  
47 Oceanus Procellarum and the northern edge of Mare Frigoris<sup>5</sup> (Fig. 1a; Extended Data Fig. 1).  
48 However, these arcuate segments span only a fraction of the circumference of the proposed  
49 basin, requiring that much of the proposed topographic rim was destroyed or modified beyond  
50 recognition.

51 In this study, we use data from NASA's GRAIL mission<sup>8</sup> to examine the subsurface  
52 structure of the Procellarum region. Bouguer gravity data (gravity field corrected for the  
53 contributions of surface topography) and gravity gradients (second horizontal derivatives of the  
54 Bouguer potential<sup>14</sup>) reveal a distinctive pattern of anomalies surrounding the region (Fig. 1b-c).  
55 These narrow belts of negative gravity gradients and positive gravity anomalies indicate narrow  
56 zones of positive density contrast in the subsurface. Previous work revealed a population of  
57 narrow, randomly oriented, ancient igneous intrusions that lack surface expressions<sup>14</sup>. In  
58 contrast, the PKT border anomalies are broader features that are spatially associated with the  
59 maria and appear to be part of an organized large-scale structure. These anomalies are the  
60 dominant features not associated with impact basins in the global gravity gradients, but only a  
61 portion of the western border anomalies in Oceanus Procellarum were noted in earlier gravity  
62 studies<sup>15</sup>.

63 To investigate the source of the anomalies, we first inverted the gravity field in the  
64 spherical harmonic domain under the assumption that the anomalies arise from variations in the  
65 thickness of both the maria and the underlying feldspathic crust (see online-only Methods for  
66 details). We focus here on two models to illustrate the range of solutions: the first imposes an

67 isostatic condition on the pre-mare crust, and the second forces the amplitude of the relief along  
68 the mare-crust and crust-mantle interfaces to be equal and opposite in magnitude. For these two  
69 models, the average structure across two of the border anomalies at the northwest corner of the  
70 PKT suggest the presence of elongated mare-filled depressions in the feldspathic crust having  
71 widths of  $\sim 150$  km and depths of 2–4 km, and underlain by crust-mantle interfaces that are  
72 shallower than adjacent areas by 3–6 km (Fig. 2e-h; Extended Data Figs 2-3). If we instead  
73 assume that the PKT border anomalies arise from igneous intrusions in the subsurface<sup>14</sup>,  
74 inversions of the average gravity profiles across these two anomalies yield widths of  $66_{-6}^{+5}$  and  
75  $82_{-36}^{+19}$  km and vertical extents of  $8_{-1}^{+1}$  and  $6_{-1}^{+3}$  km for intrusions with elliptical cross-sections,  
76 assumed density contrasts of  $550 \text{ kg/m}^3$ , and bottom depths of 25 km (Fig. 2c-d; see Methods).

77 The spherical harmonic inversion solutions are consistent with thickening of the maria over  
78 linear depressions formed by crustal thinning, as could occur in volcanically flooded rift  
79 valleys<sup>16</sup>. The branching of anomalies of the western border structure and the triple-junction  
80 intersections at some corners are consistent with the attributes of planetary rifts. This  
81 interpretation is also supported by the broad elongated depressions surrounding the border  
82 anomalies beneath Mare Frigoris and western Mare Tranquilitatis, and the scarps found in the  
83 highlands adjacent to some of the border anomalies<sup>5</sup>. The inferred crustal thinning could arise  
84 from extension of the crust by 8–18 km (Extended Data Table 1). For the intrusion models, the  
85 large widths of the inferred intrusions (greatly exceeding the vertical dimensions), and the  
86 association of the gravity anomalies with mare basalts at the surface, suggest that dike-like  
87 intrusions are not solely responsible for the anomalies. A combination of crustal thinning, mare  
88 thickening, and intrusion by dike swarms provides the most likely explanation for the anomalies.  
89 The elevated heat flux in the PKT<sup>10</sup> coupled with passive mantle upwelling during rifting would

90 have led to widespread partial melting of the underlying mantle<sup>16</sup>, so extensional tectonics would  
91 have been accompanied by dike intrusion and volcanism. These dikes may represent the magma  
92 plumbing system that provided conduits connecting deep magma reservoirs to many of the  
93 nearside maria.

94 The PKT border structures are the only known lunar structures consistent with large-scale  
95 rifting of the crust, a process more common on Earth, Venus, and Mars. The surface exposures  
96 of the maria overlying the border structures formed  $3.51 \pm 0.25$  billion years ago (Ga; area-  
97 weighted mean and standard deviation)<sup>17</sup>, representing the final stages of the volcanic infilling of  
98 the structures. In contrast, the rest of the nearside maria exhibit a range of ages of 1.2–4.0 Ga.  
99 Volcanic infilling of the rifts may have been a self-limiting process because the flexural response  
100 to the loading would have caused compression in the upper lithosphere, possibly closing off the  
101 magma conduits. This inference is supported by the observation of wrinkle ridges overlying and  
102 parallel to the border structures. Parallel wrinkle ridges flanking the Mare Frigoris border  
103 structure may also reflect structural control of the wrinkle ridges by buried tectonic structures.

104 In a polar projection centred on the PKT, the border structures delineate a quasi-  
105 rectangular shape (Fig. 3). The arcuate scarps at the edges of Maria Frigoris and Procellarum  
106 that were previously interpreted as rim segments of a Procellarum basin are seen in the GRAIL  
107 data to be a small fraction of this continuous set of well-expressed structures that trace out a  
108 polygonal pattern consisting of predominantly straight sides and angular intersections (Extended  
109 Data Fig. 1). The northeast and northwest corners of the structure deviate from the proposed  
110 circular rim<sup>5</sup> by 215 km and 175 km, respectively. Only the discontinuous and poorly expressed  
111 anomalies in the southwest portion of the region are compatible with a circular rim. This quasi-

112 rectangular pattern is in contrast with the circular or elliptical shapes of all other large impact  
113 basins<sup>9</sup>, including the hemisphere-scale Borealis basin on Mars, for which a continuous elliptical  
114 basin rim can be traced in topography and gravity data<sup>18</sup>. The interpretation of the PKT border  
115 structures as the rim of an impact basin would require hundreds of kilometres of horizontal  
116 deformation with large strain gradients to produce the angular corners. No evidence of such  
117 large-magnitude strain exists on the Moon<sup>19</sup>. Furthermore, the negative gravity gradients of the  
118 border structures do not match the signatures of known impact basins, such as the Imbrium and  
119 South Pole-Aitken basins, which are characterized by paired positive and negative gradients of  
120 equal amplitude flanking the rims and negative gradients throughout the basin interiors.  
121 Although it is not possible to disprove the existence of an ancient degraded Procellarum basin  
122 that lacks a clear geophysical signature, the geometry and gravitational signature of the structures  
123 bordering the PKT do not support the interpretation that they mark the rim of a basin.

124         The formation and geometric pattern of the PKT border structures require an explanation.  
125 Although the gravity anomalies are consistent with either lava-flooded rift valleys or dense  
126 swarms of dikes, both interpretations require substantial extension across the border structures.  
127 The location of the structures at the edge of the PKT suggests that the elevated heat flux in this  
128 region<sup>10</sup> may have played a role in the extension inferred from the gravity modelling. In a state of  
129 thermal equilibrium, both the temperature and the rate of change in temperature in the  
130 lithosphere would be linearly proportional to the concentration of heat-producing elements in  
131 and/or beneath the crust. Thus, although the PKT was always warmer than its surroundings due  
132 to the high concentrations of heat-producing elements, it would have cooled at a greater rate due  
133 to declining radiogenic heat production<sup>10</sup>. The cooling lithosphere would then have experienced  
134 thermal contraction, which in turn would have caused horizontal extension at the margins.

135 Cooling by 600 K across a region 2000 km wide would have induced the equivalent of ~8 km of  
136 extension. We tested this hypothesis with a simple model of the thermal evolution and resultant  
137 stresses (see Methods). A finite difference model was used to represent the conductive thermal  
138 evolution of the Moon, given the equivalent of 10 km of KREEP basalt at the base of a 40-km-  
139 thick crust within a spherical cap 2000 km in diameter<sup>10,11</sup>. The model predicts a temperature  
140 decrease of the PKT relative to its surroundings of >600 K between 4.0 and 3.0 Ga, with the  
141 maximum cooling at the base of the crust (Fig. 4a; Extended Data Figs 4-5).

142 The stresses resulting from the thermal contraction of the lithosphere between 4.0 and 3.0  
143 Ga were calculated with an elastic finite element model<sup>20</sup>. The far-field stresses on the opposite  
144 side of the planet were subtracted in order to isolate the effects of the PKT, since the mean stress  
145 in the lithosphere may have been affected by global contraction or expansion<sup>14,21</sup>. Cooling and  
146 contraction of the lower lithosphere within the PKT caused extension, which induced  
147 compression in the elastically-coupled upper lithosphere inside the PKT, and extension  
148 throughout the lithosphere at the edge of the PKT (Fig. 4c). Similar results were obtained if the  
149 KREEP-rich material was distributed throughout the crust (Extended Data Figs 6-7). This  
150 extension may have been augmented by an early period of global expansion<sup>14</sup>.

151 Many of the maria not associated with impact basins are found over the PKT border  
152 structures. Rise of magma to the surface in dikes requires the most tensile stress to be horizontal,  
153 as well as a vertical gradient in stress conducive to magma ascent<sup>22</sup>. The model predicts that the  
154 extensional zone bordering the PKT was conducive to magma ascent in dikes (Fig. 4d). In  
155 contrast, compressional stresses in the upper lithosphere within the centre of the PKT would tend  
156 to inhibit the rise of magma, except where this stress field was modified by later processes such

157 as impacts or loading and flexure of the lithosphere, or where magma ascent was aided by  
158 volatile exsolution or a pressurized magma chamber.

159 In order to form the observed rectilinear pattern of structures, it is necessary to break the  
160 azimuthal symmetry assumed in the model. Volumetric contraction beneath a free surface  
161 generates fracture patterns with characteristic corner angles of  $120^\circ$ . This pattern results in six-  
162 sided polygons at scales ranging from 1-100's of cm (e.g., mud cracks, columnar joints in  
163 basalt), to 1-100 m (e.g., thermal contraction polygons in permafrost), to 10 km (e.g., polygons  
164 from sediment compaction in the lowlands of Mars<sup>23</sup>). However, as the size of the structure  
165 becomes large relative to the radius of the planet, surface curvature becomes important. A  
166 polygon with  $120^\circ$  corner angles will have five or four sides when the lengths of the sides reach  
167  $32^\circ$  or  $80^\circ$  of arc, respectively. The mean length of the PKT border structures is 2150 km or  $71^\circ$ ,  
168 and the angles of the vertices range from  $109^\circ$  to  $125^\circ$ . Thus, at the scale of the PKT, a set of  
169 linear rifts intersecting at  $120^\circ$ -angle junctions around a contracting cap may result in a quasi-  
170 rectangular structure.

171 We note a similarity in the pattern of structures to the south polar terrain (SPT) of Saturn's  
172 icy moon Enceladus (Fig. 3; Extended Data Fig. 8)<sup>24,25</sup>. Both the PKT and SPT are bordered by  
173 quasi-rectangular sets of tectonic belts with angular intersections that sometimes take the form of  
174 triple junctions. Both structures enclose regions approximately  $70$ - $80^\circ$  in diameter of low  
175 topography<sup>1,25</sup>, enhanced volcanic activity<sup>10,24</sup>, and strongly elevated heat flow<sup>10,26</sup>. However, we  
176 emphasize that there are important differences between the specific processes at work and the  
177 evolutionary histories of these two very different terrains – including the tidal source of the heat,  
178 the prevalence of compressional tectonism<sup>24,25</sup>, the likelihood of a subsurface ocean<sup>27</sup>, and the



179 possibility of a mobile lithosphere<sup>28</sup> on Enceladus. Nevertheless, the gross morphological and  
180 geophysical similarities between the PKT on the Moon and the SPT on Enceladus suggest the  
181 possibility of broad parallels in their geodynamic evolution, and that similar parallels may exist  
182 with other magmatic-tectonic centres (e.g., the northern lowlands of Mercury, an irregular  
183 depression  $\sim 80^\circ$  in diameter<sup>29</sup> that has experienced widespread volcanic resurfacing<sup>30</sup>).

184

## 185 **METHODS SUMMARY**

186 Gravity gradients were calculated from the GRAIL Extended Mission gravity model  
187 GRGM900b with the SHTOOLS toolkit (available on-line at [shtools.ipgp.fr](http://shtools.ipgp.fr)). Spherical  
188 harmonic modelling of the mare and crustal thicknesses utilized SHTOOLS. The thermal models  
189 used a finite difference model of heat transfer for assumed concentrations of heat-producing  
190 elements in the PKT, crust, and mantle. Finite element modelling was conducted with the  
191 TEKTON code in an axisymmetric spherical geometry to examine the elastic stresses in the  
192 lithosphere.

193

194 **Online Content** Any additional Methods and Extended Data display items are available in the online version of the  
195 paper; references unique to these sections appear only in the online paper.

196

## 197 **Acknowledgements**

198 The GRAIL mission is a component of the NASA Discovery Program and is performed under contract to the  
199 Massachusetts Institute of Technology and the Jet Propulsion Laboratory, California Institute of Technology. J.C.A.-  
200 H. was supported by grant NNX12AL20G from NASA's GRAIL Guest Scientist Program.

201

202 **Author contributions**

203 J.C.A.-H. performed the data analyses and modelling. M.T.Z. is the principal investigator of the GRAIL mission.

204 All authors contributed to the interpretation of the results and their implications.

205

206 **Additional information**

207 Reprints and permissions information is available on-line at <http://npg.nature.com/reprintsandpermissions>.

208 Correspondence and requests for materials should be addressed to J.C.A.-H. ([jcahanna@mines.edu](mailto:jcahanna@mines.edu)).

209

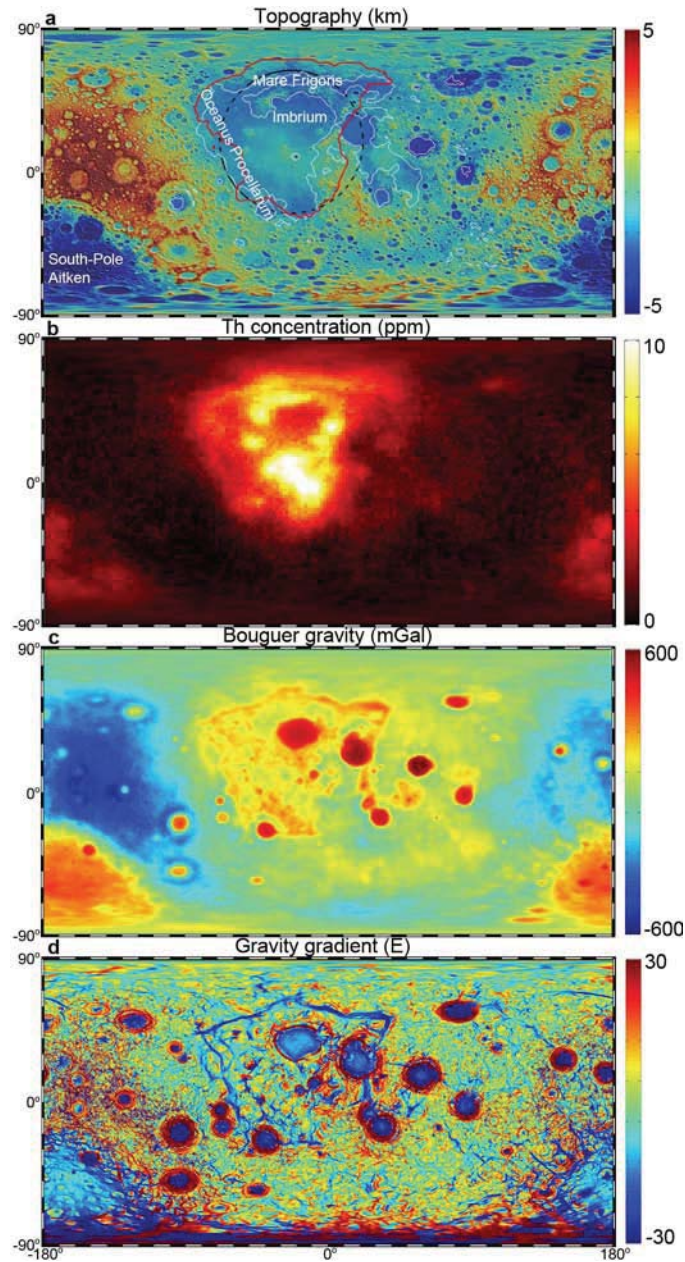
210 **Author Information**

211 Reprints and permissions information is available at [www.nature.com/reprints](http://www.nature.com/reprints). The authors declare no competing

212 financial interests. Readers are welcome to comment on the online version of the paper. Correspondence and

213 requests for materials should be addressed to J.C.A.-H. ([jcahanna@mines.edu](mailto:jcahanna@mines.edu)).

214



214

215 **Figure 1. Global maps of (a) topography, (b) Th concentration, (c) Bouguer gravity**

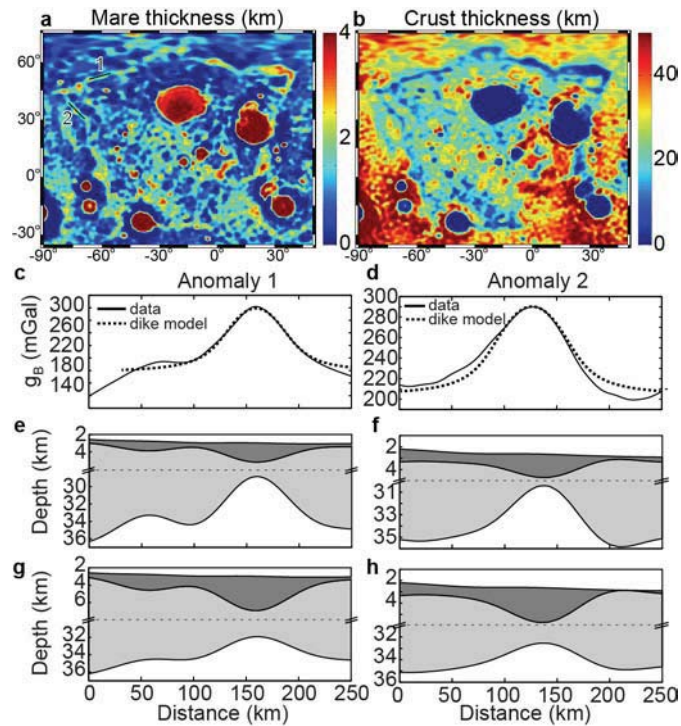
216 **anomaly, and (d) gravity gradients on the Moon.** All maps are simple cylindrical projections

217 centred on the nearside. The circular rim of the proposed Procellarum impact basin<sup>5</sup> (black

218 dashed line), the outline of the maria (white lines<sup>17</sup>), and the extent of the PKT (red line,

219 corresponding to a Th concentration of 3.5 ppm; ref. 4) are shown in **a**. Features discussed in the

220 text are labelled in **a**.



221

222 **Figure 2. Gravity and subsurface structure of the PKT border structures.** **a-b**, Maps of the

223 modelled thickness of the maria and underlying feldspathic crust. **c-d**, Average Bouguer gravity

224 profiles perpendicular to border anomalies 1 and 2 (see panel **a** for locations). **e-h**, Average

225 cross-sections of the model results orthogonal to the border anomalies showing the mare (dark

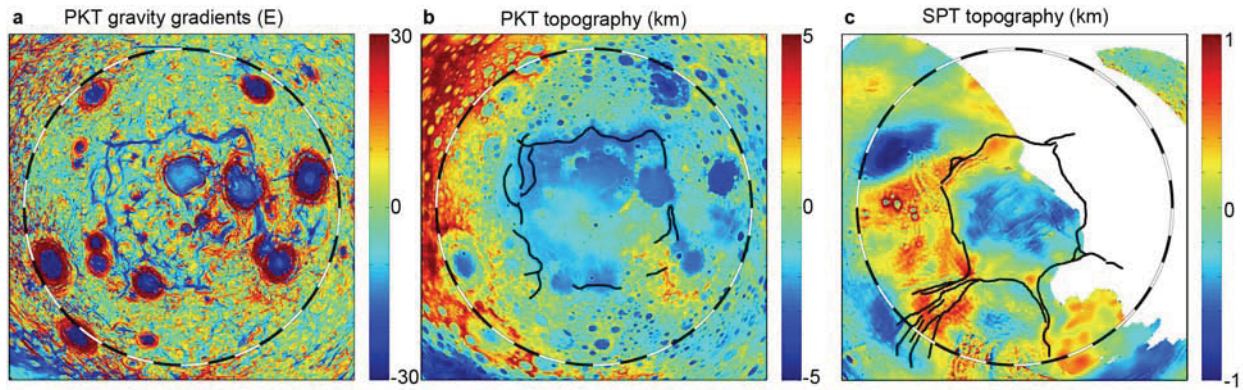
226 grey) and feldspathic crust (light grey) for two different sets of filters. The models in **e-f** impose

227 the condition that the relief along the interfaces was in isostatic equilibrium prior to infilling by

228 mare basalt, whereas the models in **g-h** impose the condition that the relief along the interfaces

229 was equal and opposite in amplitude (see Methods for further details and Extended Data Fig. 3

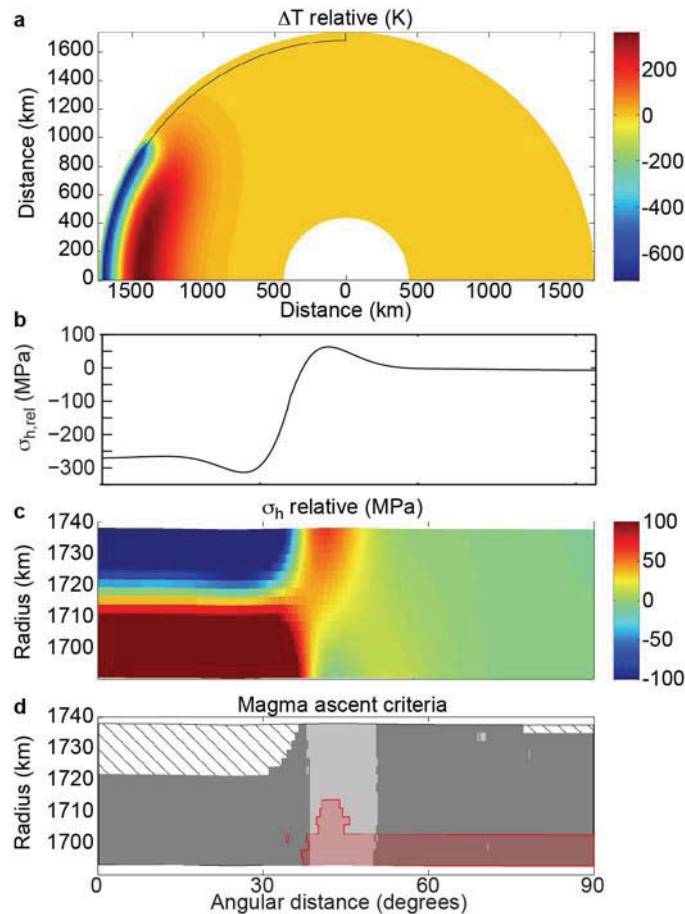
230 for results from additional models).



231

232 **Figure 3. Geometric pattern of the Procellarum KREEP terrane (PKT) border structures,**  
 233 **with a comparison to the Enceladus south polar terrain (SPT).** **a**, The border structures of  
 234 the PKT highlighted by the gravity gradients trace out a quasi-rectangular pattern, enclosing **b**, a  
 235 broad region of low elevations<sup>1</sup>. **c**, The SPT is similarly a region of low elevation<sup>25</sup> and high heat  
 236 flow<sup>26</sup> (Extended Data Fig. 8) surrounded by a quasi-rectangular pattern of border structures. All  
 237 maps are in a simple polar projection. In all panels, the circle corresponds to an angular diameter  
 238 of 180° of surface arc, divided into 10° increments.

239



239

240 **Figure 4. Predicted temperature and stress for the Procellarum region.** **a**, Predicted  
 241 temperature change of the PKT relative to its surroundings between 4.0 and 3.0 Ga. The  
 242 Procellarum region is centred on the pole on the left side of the figure. The black line denotes  
 243 the area expanded in panels **c** and **d**. **b**, In-plane horizontal elastic stress radial to the centre of  
 244 the PKT at the surface predicted by the finite element model (where positive stresses are tensile;  
 245 the far-field stress profile has been subtracted to calculate the relative stresses). **c**, Cross-section  
 246 of the in-plane horizontal elastic relative stress. **d**, Predicted zones of magma ascent; dark grey  
 247 indicates horizontal extension conducive to vertical dike formation, light grey indicates both  
 248 horizontal extension and a vertical stress gradient more favourable to magma ascent than in the  
 249 lithosphere far from the PKT, and red indicates areas in which magma will rise unassisted by

250 other factors. Cross-hatching indicates regions in which none of the criteria for magma ascent are  
251 met. The temperatures in **a** and stresses in **b,c** are both taken relative to the far-field values in the  
252 opposite hemisphere.

253

## 254 **References.**

- 255 <sup>1</sup> Smith, D. E. et al., Initial observations from the Lunar Orbiter Laser Altimeter (LOLA).  
256 *Geophys. Res. Lett.* **37**, L18204, doi:10.1029/2010GL043751 (2010).
- 257 <sup>2</sup> Wieczorek, M. A. et al., The crust of the Moon as seen by GRAIL. *Science* **339**, 671–  
258 675, doi:10.1126/science.1231530 (2013).
- 259 <sup>3</sup> Jolliff, B. L. et al., Major lunar crustal terranes: Surface expressions and crust-mantle  
260 origins. *J. Geophys. Res.* **105**, 4197–4216 (2000).
- 261 <sup>4</sup> Lawrence, D. J. et al., Global elemental maps of the Moon: The Lunar Prospector  
262 gamma-ray spectrometer. *Science* **281**, 1484–1489 (1998).
- 263 <sup>5</sup> Whitaker, E. A., The lunar Procellarum basin, in *Multi-ring Basins: Formation and*  
264 *Evolution*, edited by R. B. Merrill and P. H. Schultz, *Lunar Planet. Sci.* **12A** (Lunar and  
265 Planetary Institute, Houston, Tex., 1980), pp. 105–111.
- 266 <sup>6</sup> Cadogan, P. H., Oldest and largest lunar basin? *Nature* **250**, 315–316 (1974).
- 267 <sup>7</sup> Wilhelms, D. E., The geological history of the Moon. *U.S. Geological Survey*  
268 *Professional Paper* **1348**, 302 pp. (1987).
- 269 <sup>8</sup> Zuber, M. T. et al., Gravity field of the Moon from the Gravity Recovery and Interior  
270 Laboratory (GRAIL) mission. *Science* **339**, 668–671, doi:10.1126/science.1231507  
271 (2013).

272 <sup>9</sup> Andrews-Hanna, J. C. and Zuber, M. T., Elliptical craters and basins on the terrestrial  
273 planets, in *Large Meteorite Impacts and Planetary Evolution IV*, edited by R. L. Gibson  
274 and W. U. Reimold, Special Paper 465 (Geological Society of America, Boulder, Colo.,  
275 2010), pp. 1–13.

276 <sup>10</sup> Wieczorek, M. A. and Phillips, R. J., The "Procellarum KREEP Terrane": Implications  
277 for mare volcanism and lunar evolution. *J. Geophys. Res.* **105**, 20,417–420,430 (2000).

278 <sup>11</sup> Grimm, R. E., Geophysical constraints on the lunar Procellarum KREEP Terrane. *J.*  
279 *Geophys. Res. Planets* **118**, 768–777, doi:10.1029/2012JE004114 (2013).

280 <sup>12</sup> Laneuville, M., Wieczorek, M. A., Breuer, D., and Tosi, N., Asymmetric thermal  
281 evolution of the Moon. *J. Geophys. Res. Planets* **118**, doi:10.1002/jgre.20103 (2013).

282 <sup>13</sup> Nakamura, R et al., Compositional evidence for an impact origin of the Moon's  
283 Procellarum basin. *Nat. Geosci.* **5**, 775–778 (2012).

284 <sup>14</sup> Andrews-Hanna, J. C. et al., Ancient igneous intrusions and early expansion of the Moon  
285 revealed by GRAIL gravity gradiometry. *Science* **339**, 675–678,  
286 doi:10.1126/science.1231753 (2013).

287 <sup>15</sup> Scott, D. H., The geologic significance of some lunar gravity anomalies. *Proc. Lunar Sci.*  
288 *Conf.*, **5<sup>th</sup>**, 3025–3036 (1974).

289 <sup>16</sup> White, R. and McKenzie, D., Magmatism at rift zones: The generation of volcanic  
290 continental margins and flood basalts. *J. Geophys. Res.* **94**, 7685–7729 (1989).

291 <sup>17</sup> Hiesinger, H. et al., Ages and stratigraphy of lunar mare basalts in Mare Frigoris and  
292 other nearside maria based on crater size-frequency distribution measurements. *J.*  
293 *Geophys. Res.* **115**, E03003, doi:10.1029/2009JE003380 (2010).



294 <sup>18</sup> Andrews-Hanna, J. C., Zuber, M. T., and Banerdt, W. B., The Borealis basin and the  
295 origin of the martian crustal dichotomy. *Nature* **453**, 1212–1215 (2008).

296 <sup>19</sup> Watters, T. R. and Johnson, C. L., Lunar tectonics, in *Planetary Tectonics*, edited by T.  
297 R. Watters and R. A. Schultz (Cambridge University Press, Cambridge, 2010), pp. 121–  
298 182.

299 <sup>20</sup> Melosh, H. J. and Raefsky, A., The dynamical origin of subduction zone topography.  
300 *Geophys. J. Roy. Astron. Soc.* **60**, 333–354 (1980).

301 <sup>21</sup> Solomon, S. C., The relationship between crustal tectonics and internal evolution in the  
302 Moon and Mercury. *Phys. Earth Planet. Inter.* **15**, 135–145 (1977).

303 <sup>22</sup> McGovern, P. J., Rumpf, M. E., and Zimbelman, J. R., The influence of lithospheric  
304 flexure and volcano shape on magma ascent at large volcanoes on Venus, *J. Geophys.*  
305 *Res.* **118**, doi:10.1002/2013JE004455 (2013).

306 <sup>23</sup> Hiesinger, H. and Head, J. W., Characteristics and origin of polygonal terrain in southern  
307 Utopia Planitia, Mars: Results from Mars Orbiter Laser Altimeter and Mars Orbiter  
308 Camera data. *J. Geophys. Res.* **105**, 11,999–912,022 (2000).

309 <sup>24</sup> Porco, C. C. et al., Cassini observed the active south pole of Enceladus. *Science* **311**,  
310 1393–1401 (2006).

311 <sup>25</sup> Schenk, P. M. and McKinnon, W. B., One-hundred-km-scale basins on Enceladus:  
312 Evidence for an active ice shell. *Geophys. Res. Lett.* **36**, L16202,  
313 doi:10.1029/2009GL039916 (2009).

314 <sup>26</sup> Howett, C. J. A., Spencer, J. R., Pearl, J., and Segura, M., High heat flow from  
315 Enceladus' south polar region measured using 10–600 cm<sup>-1</sup> Cassini/CIRS data. *J.*  
316 *Geophys. Res.* **116**, E03003, doi:10.1029/2010JE003718 (2011).

317 <sup>27</sup> Behouňková, M., Tobie, G., Choblet, G., and Cadek, O., Tidally-induced melting events  
318 as the origin of south-pole activity on Enceladus. *Icarus* **219**, 655–664 (2012).

319 <sup>28</sup> O'Neil, C. and Nimmo, F., The role of episodic overturn in generating the surface  
320 geology and heat flow on Enceladus. *Nature Geosci.* **3**, 88–91 (2010).

321 <sup>29</sup> Zuber, M. T. et al., Topography of the northern hemisphere of Mercury from  
322 MESSENGER laser altimetry. *Science* **336**, 217–220, doi:10.1126/science.1218805  
323 (2012).

324 <sup>30</sup> Head, J. W. et al., Flood volcanism in the northern high latitudes of Mercury revealed by  
325 MESSENGER. *Science* **333**, 1853–1856 (2011).

326

## 326 **Methods**

### 327 **Gravity gradients**

328 Gravity data was analyzed from gravity model GRGM900b obtained from observations  
329 during the primary and extended GRAIL missions. The Bouguer gravity anomaly model was  
330 generated for an assumed a crustal density of 2550 kg/m<sup>3</sup> (ref. 2). The Bouguer gravity gradients  
331 were calculated in the spherical harmonic domain<sup>31</sup> using the software archive SHTOOLS (freely  
332 available on-line at [shtools.ipgp.fr](http://shtools.ipgp.fr)). The eigenvalues of the horizontal gravity gradient tensor  
333 ( $G_{11}$ ,  $G_{22}$ ), representing the values of the maximum and minimum curvature of the potential field  
334 at each point, were then calculated. As was done previously<sup>14</sup>, the eigenvalues were combined  
335 into a single value (the maximum-amplitude horizontal gradient, or  $G_{hh}$ ) representing the second  
336 horizontal derivative of maximum amplitude at each point on the surface:

337

$$338 \quad \Gamma_{hh} = \begin{cases} \Gamma_{11} & \text{if } |\Gamma_{11}| > |\Gamma_{22}| \\ \Gamma_{22} & \text{if } |\Gamma_{11}| \leq |\Gamma_{22}| \end{cases}$$

339

340 where  $|x|$  indicates the absolute value of  $x$ . This maximum-amplitude horizontal gradient  
341 represents the gradient orthogonal to any structures that dominate the local gravity, regardless of  
342 their orientation. The gravity gradients are given in units of Eötvös ( $1 E = 10^{-9} \text{ s}^{-2}$ ). The gravity  
343 gradients were used to reveal the presence of discrete subsurface structures, whereas the Bouguer  
344 gravity anomaly and potential were used in all subsequent analyses.

345 In this representation of the gravity gradients, a positive density anomaly will produce a  
346 negative gravity gradient, whereas a step function density anomaly will produce a symmetric pair  
347 of positive and negative gravity gradients flanking the step. For this reason, the mantle uplift  
348 beneath large impact basins is expressed as an outer ring of positive gravity gradients and an

349 inner ring of negative gravity gradients. Thus, although some of the border structures are near  
350 the edges of the overlying maria, the gravity gradient signatures are not consistent with the  
351 anomalies expected to arise from edge effects of the maria. Furthermore, the northern border  
352 anomaly is approximately centred within Mare Frigoris, and the western border structure exhibits  
353 three branches that are offset from the edge of the overlying Oceanus Procellarum by as much as  
354 600 km. The average Bouguer gravity profiles perpendicular to the border structures reveal  
355 narrow positive Bouguer anomalies (Fig. 2c,d). The elongated negative gravity gradients and  
356 positive Bouguer gravity anomalies bordering the Procellarum KREEP Terrane (PKT) are most  
357 simply explained by elongated positive density anomalies.

358 In previous work focusing on narrower structures in the lunar gravity gradient field  
359 interpreted as giant dikes or swarms of dikes, we calculated the gradients using a high-pass filter  
360 at degree and order 50, which emphasized shorter-wavelength structures<sup>14</sup>. The focus of the  
361 present work is on the longer-wavelength border anomalies surrounding the PKT, which have  
362 significant power at degrees less than 50. Thus, the gravity gradients were calculated between  
363 degrees 2 and 400, with a cosine-shaped taper applied between degrees 350 and 400. Two of the  
364 border anomalies in the northwest part of the region coincide with ancient igneous intrusions  
365 identified in the previous study of the short-wavelength gravity gradients<sup>14</sup>. However, the  
366 majority of the giant dikes identified in that study are narrower structures that lack a surface  
367 expression and are distributed randomly across the planet<sup>14</sup>. In contrast, the PKT border  
368 anomalies are longer-wavelength structures that occur within the maria and appear to be part of a  
369 large-scale organized structure.

370 In order to highlight the true shape of the PKT border anomalies, the Bouguer gravity  
371 data and gradients were plotted in a simple polar projection, preserving the distance between

372 each point and the origin, and thus preserving the shape of features centred on the origin. The  
373 global Bouguer gravity gradient map in cylindrical projection (Fig. 1) appears to show a  
374 pentagonal structure encompassing the PKT. However, re-projection in a polar projection  
375 centred on the region (Fig. 3a) reveals that the structure as a whole is dominantly quasi-  
376 rectangular. The pentagonal appearance in the cylindrical projection is a result of both the  
377 distortions at high latitude in that projection and a kink in the northern border structure at its  
378 mid-point.

379         A previous study<sup>5</sup> mapped possible ring structures associated with the Procellarum basin  
380 on a Lambert azimuthal equal-area map of the nearside of the Moon. A comparison of the  
381 GRAIL gravity gradients with this map (Extended Data Fig. 1) reveals that the majority of the  
382 mare shorelines and major scarps identified in that study parallel the Procellarum border  
383 anomalies, and a significant fraction of the wrinkle ridges overlie the border anomalies.  
384 However, the angular corners apparent in the gravity gradients are missing or rounded off in the  
385 mapped surface structures. The scarps and mare shorelines adjacent to the border anomalies are  
386 consistent with their interpretation as lava-flooded rifts, and the alignment of wrinkle ridges over  
387 the border anomalies is consistent with the flexural stresses expected to arise from the narrow  
388 loads inferred from the gravity data. The tracing of these structures on a Lambert azimuthal  
389 equal-area map, which does not preserve angles and causes significant distortions around the  
390 edges due to the non-linear radial distance scale, contributes to the apparent circularity of the  
391 structures. This distortion is particularly prominent for the northwest corner of the PKT border  
392 structures, which occurs near the limb of the Moon where the distortion is at its greatest.  
393 Nevertheless, even in this projection the border anomalies clearly delineate a polygonal structure.  
394 A simple polar projection centred on the Procellarum region preserves the distance from the

395 center to all points and thus provides a more accurate depiction of shapes centered on the origin.  
396 Only the discontinuous structures in the southwest corner of the Procellarum region are  
397 consistent with a circular pattern.

398

### 399 **Gravity inversions**

400 Long-wavelength Bouguer gravity anomalies on the Moon are thought to arise largely  
401 from variations in the relief along the crust-mantle interface<sup>2,32</sup>. In contrast, because the  
402 gravitational potential of short-wavelength anomalies attenuates rapidly with elevation, most of  
403 the observed high-degree power in the Bouguer gravity must arise at depths shallower than the  
404 crust-mantle interface. At intermediate degrees, the origin of the gravity anomalies depends on  
405 the geodynamic setting. For the case of the PKT, the vast majority of the border anomalies occur  
406 beneath maria, and thus the anomalies likely arise at least in part from variations in the relief  
407 along the mare-crust interface. However, some minor branches extend off from the main border  
408 anomalies into the surrounding crust outside the maria, suggesting that at least some component  
409 of intrusive dikes and/or uplifted crust-mantle interface contributes to the anomalies. We  
410 consider both possibilities in our analysis.

411 The width of the gravity anomalies and their association with mare basalts at the surface  
412 suggest that the anomalies may be the result of local thickening of the maria above linear  
413 tectonic structures and/or uplift of the crust-mantle interface beneath those structures. To  
414 investigate this scenario, we inverted the gravity data in the spherical harmonic domain by  
415 downward continuing the Bouguer gravity to the appropriate radii and iteratively solving for the  
416 spherical harmonic coefficients describing the relief along the density interfaces of interest,  
417 taking into account the finite-amplitude effects of that relief<sup>32</sup>. This approach has been applied

418 previously for calculating the relief along the crust-mantle interface<sup>2,32</sup>, but here we wish to solve  
 419 for the relief along both the mare-crust and crust-mantle interfaces. We first calculated the  
 420 Bouguer gravity using the density of mare basalt, since the maria comprise the top layer in our  
 421 three-layer model (mare, crust, and mantle). We adopt a mare density of  $\rho_m=3150 \text{ kg/m}^3$ , based  
 422 on the average of measured densities of Apollo mare samples<sup>33</sup>. The Bouguer anomaly was then  
 423 used to calculate the relief along the mare-crust and crust-mantle interfaces.

424 The solution for the relief along two different subsurface density interfaces is inherently  
 425 non-unique. In order to capture a range of possible solutions, we consider different filters to  
 426 parse the gravity anomalies between the crust-mantle interface and the mare-crust interface. We  
 427 designed a filter  $w_l$  to allow us to specify the desired ratio,  $f$ , between the relief along the crust-  
 428 mantle interface and that along the mare-crust interface, taking into account the degree-  
 429 dependent amplification of the gravity anomalies during their downward continuation to the  
 430 mean depth of the interface of interest:

431

$$432 \quad w_l = \frac{(R_M/R_0)^{l+2}(\rho_M - \rho_c) \cdot f}{(R_m/R_0)^{l+2}(\rho_m - \rho_c) + (R_M/R_0)^{l+2}(\rho_M - \rho_c) \cdot f}$$

433

434 where  $l$  is the spherical harmonic degree,  $\rho_c$  is the density of the feldspathic crust,  $\rho_M$  is the  
 435 density of the mantle,  $\rho_m$  is the density of the mare,  $R_0$  is the mean planetary radius (1737.15 km;  
 436 ref. 1),  $R_m$  is the mean radius of the mare-crust interface, and  $R_M$  is the mean radius of the crust-  
 437 mantle interface. This filter was applied in calculating the relief along the crust-mantle interface,  
 438 and the remaining Bouguer gravity was then used to calculate the relief along the mare-crust  
 439 interface. We assumed densities of  $2550 \text{ kg/m}^3$  and  $3220 \text{ kg/m}^3$  for the crust and mantle,

440 respectively, on the basis of previous GRAIL analyses<sup>2</sup>. We assumed a mean radius of the crust-  
441 mantle interface of 1697.15 km, resulting in a mean crustal thickness of 40 km, and a mean  
442 radius of the mare-crust interface of 1736.15 km. The filters used for the models depicted in Fig.  
443 2 are shown in Extended Data Fig. 2. The first model represents the case in which the feldspathic  
444 crust was in a state of isostasy prior to infilling by the mare, leading to a ratio  $f$  of  $\rho_c/(\rho_M-\rho_c)$   
445 (Extended Data Fig. 2a). In this model, isostasy is defined using the simple criterion of equal  
446 masses in adjacent columns. If some of the volcanic infilling of the structures occurred in  
447 parallel with the extensional tectonics, the resulting load would have driven added subsidence,  
448 which would have changed the ratio between the relief along the mare-crust and crust-mantle  
449 interfaces. The second model represents the case in which the relief along the two interfaces was  
450 equal and opposite in amplitude, with  $f$  taking on a value of 1 for degrees  $>10$ . However, because  
451 the long-wavelength topography of the Moon is largely isostatic, we assumed the isostatic ratio  
452 for  $f$  for degrees 1–3, with a linear transition between the isostatic and equal amplitude values  
453 over degrees 3–10, and the equal amplitude value from degrees 10 to 125 (Extended Data Fig.  
454 2b). These two models serve to illustrate the range of possible solutions and the relative  
455 insensitivity of the inferred extension to the model assumptions. A low-pass cosine taper from  
456 degrees 125 to 150 was applied to all models.

457         The resulting models match the gravity data but do not take into account the effects of  
458 flexure, which would perturb the interface depths relative to their elevations prior to mare  
459 loading and thus alter the assumed pre-loading ratio between the relief along the interfaces.  
460 Although the models were applied globally, the results are not valid in areas outside the maria.  
461 Similarly, crustal thickness models that neglect the high density of the mare basalt and the  
462 possible variations in mare thickness will have errors within the maria. The mean radius of the



463 mare-crust interface was chosen so as to bring the base of the maria within the Procellarum  
464 region below the surface over most of the observed maria. However, the modeled long-  
465 wavelength variations in the thickness of the maria are poorly constrained because of the  
466 ambiguity between the gravitational effects of variations in the relief along the mare-crust and  
467 crust-mantle interfaces. As a result, the distribution of areas with predicted mare thicknesses  
468 greater than zero only approximately matches the observed distribution of the maria.  
469 Nevertheless, the shortwavelength variations in the thickness of the maria beneath the border  
470 anomalies are robust, given the model assumptions.

471         The density of the lunar mantle beneath the PKT is not known. The process responsible  
472 for concentrating the KREEP-rich materials on the nearside of the Moon may have also brought  
473 dense ilmenite-rich cumulates to the base of the crust on the nearside<sup>34</sup>. Overturn of the  
474 buoyantly unstable magma ocean cumulates would have mixed this material to deeper levels in  
475 the lunar mantle<sup>35,36</sup>, but this overturn is limited by the high viscosity of the solid ilmenite-rich  
476 cumulates and will only occur for a limited range of scenarios<sup>37</sup>. It is possible that a mixture of  
477 olivine and ilmenite-rich cumulates sank as solid diapirs, leaving behind a portion of the  
478 ilmenite-rich material at shallower levels<sup>37</sup>. To account for the possibility of shallow ilmenite-  
479 rich material beneath the PKT, we also consider a high-mantle-density endmember model with  
480 an assumed mantle density of 3500 kg/m<sup>3</sup>, representative of the density of the late stage  
481 crystallization products from the magma ocean<sup>36</sup>. The higher mantle density reduces the  
482 predicted mantle uplift beneath the border structures, and similarly reduces the predicted  
483 extension.

484         We also considered two additional end-member scenarios in our gravity models. For one  
485 model, we assumed that all of the gravity anomalies at degrees >10 arise from variations in the

486 thickness of the maria. This model required a mean mare-crust interface radius of  $R_0 - 6$  km in  
487 order to bring the mare-crust interface below the surface in the regions of interest. For another  
488 model, we assumed that all of the gravity anomalies at degrees  $>10$  arise from variations in the  
489 relief along the crust-mantle interface. This model became unstable at higher degrees due to the  
490 amplification of the high-degree gravity anomalies during downward continuation to the mean  
491 depth of the crust-mantle interface, so a cosine taper was applied between degrees 75 and 100 to  
492 stabilize the solution. As a result, this model is a factor of 1.6 coarser in resolution than the other  
493 models. This result provides further evidence that the short-wavelength gravity anomalies must  
494 arise from density anomalies at depths more shallow than the crust-mantle boundary. This model  
495 ascribing all of the Bouguer gravity to variations along the crust-mantle interface is comparable  
496 in resolution to the global GRAIL crustal thickness models<sup>2</sup> (low-pass filtered with an amplitude  
497 of 0.5 at degrees 87 and 80, respectively, corresponding to spatial wavelengths of 63 and 68 km).  
498 In contrast, the models ascribing a substantial fraction of the Bouguer gravity to the shallower  
499 mare-crust interface are higher in resolution (low-pass filtered with an amplitude of 0.5 at degree  
500 137, corresponding to a spatial wavelength of 40 km). For both models described above, we  
501 assumed that variations in the the top and bottom surfaces of the feldspathic crust from degrees 1  
502 to 3 were isostatically compensated before mare flooding, with a linear transition to the desired  
503 filter from degrees 3 to 10. These final two models are not likely to be accurate representations  
504 of the subsurface structure, but they bracket the range of possible solutions.

505         The predicted relief along the interfaces was used to calculate the thicknesses of the crust  
506 and maria (Extended Data Fig. 3). The broad patterns of mare thickness in this region as  
507 indicated by the models are highly uncertain, due to the non-uniqueness of the division of the  
508 gravity anomalies between the mare-crust interface and the crust-mantle interface. In some

509 areas, the predicted base of the mare rises above the surface, indicating the need for subsurface  
510 mass deficits as could arise from additional variations in the crustal thickness or density in order  
511 to explain the observed gravity within the context of this model. These errors outside the maria  
512 do not affect the predictions for the Procellarum border structures. The local thickening of the  
513 mare over the western Procellarum border structure is to first order consistent with maps of the  
514 mare thickness derived from geological constraints, such as the burial depths of impact craters,  
515 which show local thickenings of up to >1.5 km along this structure<sup>38</sup>. Models combining the  
516 effects of dikes with the relief along the mare-crust and crust-mantle interfaces would predict  
517 narrower dikes than models that ascribe the entire gravity anomaly to the presence of dikes, and  
518 reduced relief along the density interfaces relative to models without dikes.

519 The extension across the structures was calculated from the thickness of the feldspathic  
520 crust by integrating the fractional crustal thickness anomaly across the structures:

521

$$522 \quad \Delta L = \int \left( 1 - \frac{c(x)}{c_0} \right) dx$$

523

524 where  $\Delta L$  is the change in length,  $c(x)$  is the thickness of the feldspathic crust as a function of  
525 location, and  $c_0$  is the mean thickness of the crust on either side of the structure. The extension  
526 was calculated between the shoulders on either side of the rift for each model, encompassing a  
527 zone 131 and 152 km wide for anomalies 1 and 2, respectively. The calculated extension and  
528 corresponding extensional strain across the structures for each of the models are given in  
529 Extended Data Table 1. The models with an isostatic ratio between the relief at the top and  
530 bottom of the feldspathic crust predict greater extension because a larger fraction of the gravity  
531 signal is downward continued to the crust-mantle interface, resulting in greater amplification of

532 the short-wavelength anomalies. The extension calculated using the crustal thickness models is  
533 an upper bound because some contribution to the gravity anomaly arising from the mechanical or  
534 thermal reduction of the crustal porosity beneath the mare load and surrounding the intruded  
535 dikes is likely.

536 We next inverted the Bouguer gravity over the PKT border structures for the best-fit  
537 dikes using a Monte Carlo approach. The sources of the anomalies were represented as density  
538 anomalies with elliptical cross-sections in the vertical plane perpendicular to the long axes of the  
539 anomalies, of assumed density contrast and bottom depth and unknown width and top depth. The  
540 bottom depths were set to the typical crustal thickness within the PKT of ~25 km (ref. 2), and the  
541 density contrasts were set to 550 kg/m<sup>3</sup>, corresponding to a crustal density of 2550 kg/m<sup>3</sup> (ref. 2)  
542 and an intrusion density of 3100 kg/m<sup>3</sup> (ref. 33). Dikes with elliptical cross-sections were then  
543 constructed from a large number of rectangular prismatic elements, and the gravity anomaly was  
544 calculated from those prisms<sup>39</sup>. The best-fit solutions were found using a simple Markov chain  
545 Monte Carlo (MCMC) approach<sup>14</sup>. The one-standard-deviation (1- $\sigma$ ) confidence intervals on the  
546 best-fit solutions were obtained by using a Metropolis-Hastings MCMC to test 20,000 models and  
547 analyzing the histograms of the resultant model parameters<sup>14</sup>. If the volume of the dike is  
548 accommodated solely by horizontal extension, then the resulting extensions for anomalies 1 and  
549 2 are 21 km and 20 km, respectively, given intrusion into a 25-km-thick crust.

550

## 551 **Thermal modelling**

552 The thermal evolution of the PKT was modelled following earlier work by *Wieczorek*  
553 *and Phillips*<sup>10</sup> and *Grimm*<sup>11</sup>, under the assumption of conductive heat transfer through the  
554 mantle. The results of this work are primarily sensitive to the temperatures in the lithosphere,

555 which are dominated by the concentration of heat-producing elements in the crust and the  
556 conductive heat transfer through the lithosphere. Although early convection beneath the PKT  
557 was possible<sup>12</sup>, this convection would have had only a second-order effect on the temperatures in  
558 the lithosphere. We used a finite difference approach to solve the spherical axisymmetric thermal  
559 diffusion equation. The model was benchmarked against the analytic solution for half-space  
560 cooling from an instantaneous temperature change applied to the surface, as well as by  
561 comparison with the results of previous work<sup>10</sup>. The model cells were divided into crust, mantle,  
562 and KREEP components.

563         The PKT was represented by a spherical cap 2000 km (66°) in diameter in which the  
564 concentration of heat-producing elements was enhanced. The lack of similarly high  
565 concentrations of heat-producing elements on the farside is supported by the lack of evidence for  
566 KREEP-rich material within or surrounding the South Pole-Aitken impact basin<sup>3</sup>. The cause for  
567 this concentration of incompatible elements on the nearside is not known, but it may be related to  
568 a degree-1 Rayleigh-Taylor instability that arose from the gravitational instability of the dense  
569 ilmenite rich cumulates formed in the late stages of magma ocean crystallization<sup>34</sup>. The crustal  
570 thickness was set to a uniform value of 40 km in order to isolate the effect of the concentration of  
571 heat-producing elements in the PKT. The effect of the thicker crust outside of the PKT is less  
572 than the uncertainties in the concentration of heat-producing elements and the thermal  
573 conductivity of the crust and PKT. We assumed a thermal conductivity of 2.0 W/m K for the  
574 crust and KREEP-rich material, and 3.0 W/m K for the mantle. The densities of the crust/PKT  
575 and mantle were set to 2550 and 3200 kg/m<sup>3</sup>, respectively, and a specific heat of 1200 J/kg K  
576 was assumed for all materials.

577 Previous studies favoured a 10-km-thick layer of KREEP basalt at the base of the  
578 crust<sup>10,12</sup>, but other workers have argued that this scenario is not compatible with the gravity and  
579 topography of the region and generates too much melt<sup>11</sup>. In our nominal model, we included a  
580 10-km-thick layer of KREEP basalt at the base of the crust. We also considered the case of a 10-  
581 km-thick layer of KREEP basalt distributed uniformly throughout a 40-km-thick crust. We  
582 assumed a U concentration in the KREEP basalt of 3.4 ppm by weight, and concentrations of  
583 0.14 ppm and 6.8 ppb in the crust and mantle, respectively<sup>10,12</sup>. We assumed a K/U ratio of 2500  
584 and Th/U ratio of 3.7 in all materials<sup>12</sup>. The enhanced concentration of KREEP is given an abrupt  
585 edge in the thermal model for simplicity. The thermal effects of this edge are broadened over the  
586 thermal diffusion length scale (~50 km for 100 million years), whereas the stress effects are  
587 spread out over a distance comparable to the flexural half-wavelength (~540 km for a lithosphere  
588 thickness of 50 km). The overall stress pattern would be unaffected by tapering the margins of  
589 the KREEP terrane over length scales of this order. The effects of melting and melt extraction  
590 on the temperature evolution were neglected. Extraction of melt would reduce the magnitude of  
591 the thermal anomaly in early time steps and decrease the amount of cooling by a modest amount,  
592 but would not change the character of the results.

593 High temperatures throughout the lunar interior are expected after accretion and  
594 solidification of the magma ocean<sup>36</sup>. The model was initialized with an approximation of an  
595 adiabatic temperature gradient throughout the model domain<sup>10</sup>, increasing linearly from 1450 K  
596 at the surface to 1500 K at the core-mantle boundary at a radius of 438 km. This temperature  
597 profile represents the temperature at the end of an early convective period. In the absence of an  
598 early period of convection, the temperatures at the top of the mantle after magma ocean overturn  
599 would have been similar<sup>36</sup>. The top boundary condition was set to a constant temperature of 250

600 K, approximating the radiative equilibrium temperature of the lunar surface. A constant heat  
601 flux of 0 was applied as the basal boundary condition at the core-mantle boundary. The model  
602 begins at  $t=0$  (4.5 Ga) and was run forward in time for 4.5 billion years. The change in  
603 temperature with time was calculated between 4.0 Ga (somewhat before the onset of the  
604 geological record) and 3.0 Ga, bracketing the period during which the majority of the maria  
605 formed<sup>17,40,41</sup>. It is only the change in temperature that generates thermal stresses in the  
606 lithosphere, so even though the PKT was always warmer than its surroundings, its time evolution  
607 was characterized by net cooling and thermal contraction because it cooled at a faster rate. The  
608 temperature change of the PKT relative to the surroundings was also calculated for illustration  
609 purposes by subtracting the temperature profile at the antipode of the PKT. The absolute change  
610 in temperature was used in all stress modelling, but the relative temperature change serves to  
611 highlight the evolving thermal anomaly beneath the PKT.

612         The changes in temperature as functions of time at 25-km-depth (the midplane of the 50  
613 km-thick lithosphere assumed for the stress modeling) both within and outside of the PKT are  
614 shown in Extended Data Fig. 4. Both scenarios for the distribution of KREEP-rich material  
615 show similar patterns, but the model with an isolated KREEP-rich layer beneath the crust  
616 experiences an early phase of warming in the first few hundred million years. Between 4.0 and  
617 3.0 Ga, both models predict substantially more cooling in the PKT than elsewhere. The mantle  
618 immediately below the PKT follows a similar pattern of cooling with time as a result of the  
619 decline in heat production within the PKT. In contrast, the mantle at deeper levels warms up as  
620 it slowly comes into thermal equilibrium with the overlying KREEP material<sup>10</sup>. The changes in  
621 temperature of the upper and lower mantle with time are most pronounced for the case of  
622 KREEP at the base of the crust (Extended Data Fig. 5). However, the net effect of the cooling

623 upper mantle and warming lower mantle approximately cancel out. The temperature changes  
624 predicted here are somewhat larger than those of *Wieczorek and Phillips*<sup>10</sup> as a result of the  
625 different ratios between the concentrations of heat-producing elements<sup>12</sup> and the neglect of latent  
626 heat and melt extraction effects in this study. Reducing the concentration of radiogenic isotopes  
627 or taking into account melt extraction would reduce the magnitudes of the predicted temperature  
628 changes and stresses, but would not affect their spatial patterns.

629         There is substantial uncertainty in the early thermal state of the Moon. The variation of  
630 temperature with depth after accretion and solidification of the magma ocean depends strongly  
631 on the timescale of accretion<sup>42</sup>, the depth of the magma ocean<sup>21,42</sup>, and the possible gravitational  
632 overturn of the magma ocean cumulates<sup>36,37</sup>. However, our models depend primarily on the  
633 temperatures within the lithosphere, which are dominated by the time evolution of the heat  
634 production within the crust. By 4.0 Ga, at which time we begin tracking the temperature changes  
635 to calculate the strain, the effect of the assumed initial condition on the temperatures in the  
636 lithosphere is greatly reduced. The early period of thermal equilibration of the lithosphere is  
637 reflected in the ~200 million year period of increasing temperature for the case of KREEP-rich  
638 material concentrated at the base of the crust (Extended Data Fig. 4). The possible persistence of  
639 mantle convection throughout the time period of interest<sup>12</sup> would affect the distribution of  
640 temperature with depth in the mantle but would have little effect on the time evolution of the  
641 temperature in the lithosphere.

642         Both Apollo seismic observations<sup>43</sup> and GRAIL gravity observations<sup>2</sup> indicate that the  
643 Moon's upper crust is fractured and porous, possibly to a depth of ~20 km. This porosity is  
644 likely to reduce the thermal conductivity of the upper crust<sup>44</sup>. The viscous closure of porosity is a  
645 thermally activated process<sup>2,45</sup>, so the higher temperatures within the PKT (Extended Data Fig.



646 4) may have decreased the crustal porosity and increased the thermal conductivity in the PKT  
647 relative to its surroundings. This increased thermal conductivity would have acted to accelerate  
648 the cooling of the PKT relative to that shown in Extended Data Figs 4-5. We have not attempted  
649 to model this process in detail, but we note that it will positively reinforce the thermal evolution  
650 shown here.

651

## 652 **Stress modelling**

653 The stresses resulting from the changes in temperature with time were modelled using the  
654 *Tekton* finite element software<sup>20</sup> in a spherical axisymmetric geometry subject to a uniform radial  
655 gravitational acceleration. In order to provide adequate spatial resolution in the PKT, the model  
656 domain was limited to the elastic lithosphere, assumed to be 50 km thick (see discussion below).  
657 The bottom boundary condition represented the restoring force of the mantle with a pressure that  
658 varied with depth, whereas elements were free to move in both vertical and horizontal directions.  
659 The effects of the buoyant upward pressure arising from thermal anomalies in the mantle below  
660 the PKT were applied to the bottom boundary as an additional pressure term that varied with  
661 location on the basis of the thermal model results. This pressure term was calculated as the depth  
662 integral of the density contrast relative to background density, scaled by the gravitational  
663 acceleration. Although considerable thermal anomalies are predicted in the sub-lithospheric  
664 mantle beneath the PKT, the effects of the cooling upper mantle and warming lower mantle  
665 largely cancel out. The remaining pressure contributes to a broad upwarping of the surface<sup>11</sup> but  
666 has little effect on the short-wavelength stresses that are the focus of this analysis. The final  
667 topography and gravity anomalies over the PKT as a whole would have been strongly affected  
668 by the flexural resistance of the lithosphere<sup>11</sup>, the thinning of the crust within the PKT<sup>2</sup>, and

669 loading by the maria<sup>12</sup>. The excess basal pressure far from the PKT, representing the effects of  
670 net global expansion or contraction, was subtracted from the basal pressure condition throughout  
671 the model. The net volume change of the interior could add a uniform compressional or  
672 extensional horizontal stress to the lithosphere, depending on the early thermal history of the  
673 Moon<sup>14,21,42</sup>. The model domain of a 50-km-thick lithosphere stretching from pole to pole was  
674 divided into 600 nodes in the azimuthal direction and 20 nodes in the radial direction, resulting  
675 in element dimensions of 9.1 by 2.5 km at the surface.

676 The predicted temperature change between 4.0 and 3.0 Ga (Extended Data Figs 5b, d)  
677 was used to calculate the resulting instantaneous elastic stresses in the model elements prior to  
678 any deformation<sup>46</sup>:

679

$$680 \quad \sigma = \alpha_v \Delta T \frac{E}{3(1-2\nu)}$$

681

682 where  $\sigma$  is the stress (taken here to be isotropic),  $\alpha_v$  is the volumetric coefficient of thermal  
683 expansion (assumed to be  $2 \times 10^{-5} \text{ K}^{-1}$ ),  $E$  is Young's modulus (assumed to be 100 GPa, which is  
684 likely appropriate for the lower crust in which the greatest contraction occurs), and  $\nu$  is Poisson's  
685 ratio (assumed to be 0.25). These pre-strain thermal stresses were added to the lithostatic stresses  
686 for the initial condition for the finite element model. Imposing the effects of thermal contraction  
687 with the pre-strain stresses allows the resultant deformation and its effects on the stress field to  
688 arise self-consistently in the model.

689 The elastic stresses were calculated relative to the far-field values at the opposite side of  
690 the planet in order to isolate the effects of thermal contraction of the PKT. Geological and  
691 geophysical evidence suggests that the net stress state of the Moon may have evolved from

692 global expansion and extension to contraction and compression over the course of its thermal  
693 evolution<sup>14,21</sup>. In this scenario, the net global stress change at the time of formation of the border  
694 anomalies may have been small. However, theoretical models have shown that an early period of  
695 global expansion is difficult to generate for many likely lunar formation scenarios<sup>42</sup>. We put this  
696 question aside and focused instead on the local stresses within and surrounding the PKT relative  
697 to the typical stresses far from the region. These stresses would have been modified by the  
698 global stress state at the time of interest by the addition of a uniform compressional or  
699 extensional horizontal stress. In addition to the relative stresses, we also show the difference  
700 between the in-plane horizontal and vertical stresses ( $\sigma_h - \sigma_v$ ) and the deviatoric horizontal stress  
701 ( $\sigma_h - \sigma_p$ ), where  $\sigma_p$  is the pressure or mean stress value over all three directions (Extended Data  
702 Fig. 6). The width of the zone of predicted extension (~400 km) is somewhat wider than the  
703 observed border structures (~200 km), but localization of the strain release would likely have  
704 occurred if the structures are analogous to lava-flooded rifts. Similar stress patterns are predicted  
705 if KREEP-rich material is distributed uniformly through the crust, though the magnitudes of the  
706 stresses are reduced (Extended Data Fig. 7) because of the reduced temperature changes  
707 (Extended Data Fig. 5c, d).

708         The stresses predicted by the model are dominated by the simple horizontal contractional  
709 stresses within the lithosphere. However, volumetric contraction does induce small changes to  
710 the surface topography, which generates bending stresses of small magnitude. Models in which  
711 the vertical displacement was set to zero at either the top or the bottom of the model domain  
712 resulted in similar stress fields, demonstrating that bending stresses do not contribute  
713 significantly.

714           The modelling in this study is intentionally simple in order to isolate the effect of the  
715 contracting cap within the PKT. This analysis did not consider the effects of spatial or temporal  
716 variations in the lithosphere thickness. If the base of the lithosphere follows the 800°C isotherm  
717 in the dry lunar mantle<sup>47</sup>, the lithosphere thickness would range from 33 km within the PKT to  
718 216 km outside of the PKT at 3 Ga for the case of KREEP concentrated at the base of the crust,  
719 with a smaller amplitude change in lithosphere thickness for KREEP distributed throughout the  
720 crust. The adopted lithosphere thickness value of 50 km is intermediate between the predicted  
721 values within and outside of the PKT. This assumption is appropriate, since the tensile stresses  
722 of interest are at the edge of the PKT. Since the dominant source of stress is the horizontal  
723 contraction of the lithosphere within the PKT, the stresses for the case of a variable lithosphere  
724 should be similar. Models that were run with a spatially variable lithosphere thickness predicted  
725 similar results but were subject to artefacts resulting from the large distortions in the element  
726 grid at the edge of the PKT. This model represented only the elastic stresses within the  
727 lithosphere. A viscoelastic model of the lithosphere and underlying mantle would predict a  
728 viscous transition zone at the base of the lithosphere within which the stresses decreased to zero  
729 at depth. Coupling of the thermal and viscoelastic evolution would result in a lithosphere that  
730 thickens with time, and would likely reduce the magnitude of the predicted extension, but would  
731 not change the character of the results. Within the PKT, the stresses are characterized by  
732 compression in the upper lithosphere and extension in the lower lithosphere, whereas at the  
733 edges of the PKT the extensional stress reaches the surface. However, the frictional strength at  
734 the surface should approach 0 MPa, allowing release of the shallow compressional stresses.  
735 Brittle compressional failure of the frictionally weak upper lithosphere throughout the PKT

736 would allow further contraction of the spherical cap, significantly enhancing the extension at its  
737 margins.

738 In order to model directly the formation of the observed border structures, it would be  
739 necessary to localize the extension through tectonic failure. The localization of the extensional  
740 failure at discrete rift zones in the border structures would be dependent on the strain rate,  
741 rheology, and crustal thickness<sup>48</sup>. Failure at the edges of the PKT would relieve the stresses in  
742 the interior and allow the spherical cap to pull away from the surrounding lithosphere. Future  
743 work is needed to model more directly the formation of these border structures. In this work, we  
744 simply show that thermal contraction of the PKT predicts extension at its edges, providing a  
745 straightforward model for generating the PKT border structures. Additional stresses arising from  
746 uplift or subsidence of the lithosphere<sup>11,12</sup> and magmatic processes would have also likely played  
747 a role.

748 Zones favourable to the ascent of magma-filled dikes through the lithosphere were  
749 identified as those experiencing in-plane horizontal extension relative to the vertical stress and a  
750 favourable vertical stress gradient. Horizontal extension is required for the formation of vertical  
751 dikes, which would otherwise flatten out to produce horizontal sills. In addition, the upward  
752 propagation of the dikes requires that the vertical gradient in the confining horizontal stress in  
753 the lithosphere ( $d\sigma_h/dz$ , where positive stresses are tensile,  $z$  is positive upward, and  $\sigma_h$  includes  
754 both the lithostatic stress and the added tectonic stress) be greater than the hydrostatic pressure  
755 gradient in the magma, causing the lower tip of the dike to pinch shut while the upper tip  
756 propagates upward. The low density of the lunar crust<sup>2</sup> is an impediment to the rise of magma,  
757 even in a neutral stress state. Magma ascent is favoured in cases in which the upper lithosphere  
758 is in a state of extension relative to the lower lithosphere<sup>49</sup>. For a magma density of 2900 kg/m<sup>3</sup>,

759 this state corresponds to a vertical gradient in the horizontal stress in the lithosphere in excess of  
760 4.7 MPa/km. However, the stress gradient in the upper portions of a conductively cooling  
761 lithosphere with internal heat production and basal heating is generally not conducive to magma  
762 ascent as a result of the increasing horizontal extension with depth caused by the declining  
763 geothermal gradient in the lithosphere with time. This problem could be ameliorated by a failure-  
764 induced reduction in the extensional stresses in the lower crust, by volatile exsolution within the  
765 magma to enhance the driving force for magma ascent<sup>50</sup>, or by a pressurized magma reservoir at  
766 depth. We use the criterion of a vertical stress gradient >4.7 MPa/km for unassisted magma rise,  
767 and we also look at the stress gradient relative to the far-field value antipodal to the PKT to  
768 assess the relative tendency for magma to rise through the lithosphere if assisted by other factors  
769 as discussed above.

770 By these criteria, the zone at the margin of the PKT experiences stresses most conducive  
771 to magma ascent and eruption. Extensional horizontal stresses radial to the centre of the PKT  
772 would facilitate the formation of circumferential dikes throughout the full vertical extent of the  
773 lithosphere. The stress gradient in this zone is more conducive to magma ascent than anywhere  
774 else on the Moon. For the case of heating by a layer of KREEP at the base of the crust, magma  
775 would be predicted to rise unassisted to the middle of the lithosphere, whereas further ascent  
776 would require additional driving forces (Extended Data Fig. 6c). For the case of heating by  
777 KREEP distributed throughout the crust, the zone at the edge of the PKT is still the preferred  
778 location of magma ascent, but some added driving force such as volatile exsolution or a  
779 pressurized magma chamber is required for the rise of magma into the crust (Extended Data Fig.  
780 7c).

781           The model also predicts changes to the surface topography. The thermal contraction of  
782 the lithosphere with time causes surface subsidence due to the vertical component of that  
783 contraction. Additionally, the horizontal shortening of the spherical cap centred on the PKT  
784 results in further subsidence due to the effects of the membrane stresses. Taking into account  
785 both the thermal contraction of the lithospheric cap in the PKT and the effects of thermal  
786 anomalies in the mantle, our models predict changes in surface topography less than 0.5 km  
787 during the period between 4.0 and 3.0 Ga. This result cannot be directly compared with the  
788 observed topography because it represents only the change in topography over a fraction of lunar  
789 history. However, we note that the predicted elevation changes are smaller than the observed  
790 relief. The topographic depression within Procellarum cannot be explained by thermal  
791 subsidence alone.

792           Previous work found that the patterns of uplift predicted by thermal models of the PKT  
793 are difficult to reconcile with the observed long-wavelength gravity and topography<sup>11,12</sup>.  
794 However, the gravity and topography within the PKT are also likely affected by variations in the  
795 thickness of the crust and by possible density anomalies in the underlying mantle<sup>12</sup>. The low  
796 topography within the PKT may also be affected by a reduction in the porosity of the crust from  
797 thermal annealing<sup>45</sup>. For a lunar crustal porosity of 12% (ref. 2), annealing the pore space in the  
798 lower 10–20 km would reduce the surface elevation by 1.2–2.4 km, consistent with the observed  
799 relief.

800           We suggest that the quasi-rectangular pattern of border structures surrounding the PKT is  
801 consistent with the intersection of linear rifts at 120°-angle triple junctions when the effect of the  
802 curvature of the surface is taken into account. Although the PKT border structures display some  
803 intermediate kinks and intersections, the overall planform is quasi-rectangular. Similarly,

804 although small-scale contraction crack polygons of all types in nature often have highly irregular  
805 forms, in the absence of competing effects (such as progressive subdivision of the polygons) the  
806 average structure is hexagonal because of the dominance of 120°-angle triple junctions at the  
807 vertices<sup>51</sup>. At small scales, the diameter of the polygons is determined by the size of the stress  
808 shadow around the fractures, which is proportional to the depth to which the fractures  
809 propagate<sup>51</sup>. The depth of fracturing for small contraction-crack polygons on Earth is dictated by  
810 the strain rate, the variation of stress with depth, and the rheology of the material in which the  
811 fractures form<sup>51</sup>. For the PKT, the size of the polygon was likely determined instead by the  
812 diameter of the tensile stress belt at the surface surrounding the thermal anomaly. The  
813 propagation of the fractures or rifts into the interior of the region may have been prevented by  
814 the compressional stresses in the upper lithosphere above the thermal anomaly (Extended Data  
815 Figs 6–7), which may have had an effect similar to the stress shadows around fractures in small-  
816 scale polygons. The distribution of KREEP-rich material in the subsurface is poorly constrained,  
817 while the distribution on the surface is strongly affected by the ejecta of the Imbrium basin and  
818 the distribution of KREEP-rich maria (the latter of which were controlled in part by the pattern  
819 of the PKT border structures). An alternative explanation for the pattern of border structures that  
820 warrants further consideration is that the distribution of KREEP-rich material in the subsurface  
821 follows a quasi-rectangular pattern.

822

### 823 **Parallels between the PKT and the south polar terrain of Enceladus**

824 The overall planform of the PKT border structures bears a strong resemblance to that of  
825 the border structures surrounding the south polar terrain (SPT) of Saturn's icy moon Enceladus,  
826 which are also quasi-rectangular in outline<sup>25</sup>. However, as discussed in the main text and



827 expanded upon below, substantial differences exist between these provinces and their inferred  
828 evolutionary histories. We emphasize that we do not suggest that the specific processes and  
829 evolutionary paths of these two regions were identical. Rather, the gross similarities between  
830 these two provinces on different bodies suggests broad parallels in the processes governing their  
831 evolution. Here we summarize the basic properties of each province, and then discuss the SPT in  
832 more detail.

833         The PKT on the Moon is a broad area of enhanced surface heat flow as a result of the  
834 high concentrations of heat-producing elements within the KREEP-rich material<sup>3,10</sup> (Extended  
835 Data Fig. 8). This compositional anomaly is likely a result of the concentration beneath the  
836 nearside of the late-stage crystallization products of the lunar magma ocean<sup>34</sup>, including dense  
837 ilmenite-rich cumulates and KREEP-rich material with high concentrations of U, Th, and K. The  
838 PKT was the most volcanically active region on the Moon and contains the majority of the mare  
839 basalt provinces<sup>10</sup>. GRAIL gravity data has revealed the PKT to be surrounded by a quasi-  
840 rectangular set of magmatic-tectonic structures with straight sides and angular intersections. The  
841 border anomalies along the northern (Mare Frigoris) and eastern edges of the PKT occur beneath  
842 maria that are confined within elongated topographic depressions, whereas the border anomalies  
843 on the western and southern edges of the PKT lie adjacent and interior to the topographic step up  
844 to the highlands. The PKT is characterized by low topography that is largely isostatically  
845 compensated over long wavelengths. This compensated depression can be explained by a crust  
846 that is thinner<sup>2</sup> or denser than the surrounding crust, by the presence of denser materials at depth,  
847 or by a combination of these effects. Thermal annealing of the pore space beneath the PKT due  
848 to its high heat flow may have increased the bulk density of the crust at depth, which may  
849 contribute to the low topography<sup>45</sup>. Deeper density anomalies could result from either the

850 intrusion of KREEP-rich magma into the lower crust, or from the presence of a remnant of the  
851 ilmenite-rich cumulates in the upper mantle that may not have fully mixed into the deeper  
852 interior<sup>37</sup>. Although a thinner crust likely explains most of the observed topography,  
853 contributions from reduced crustal porosity and the presence of dense materials within or below  
854 the crust appear likely.

855         The SPT on Enceladus is an area of strongly enhanced surface heat flow<sup>26,52,53</sup> (Extended  
856 Data Fig. 8) as a result of either localized tidal heating or the localized release of global tidal  
857 heating. The source of this thermal anomaly is thought to be related to the presence of a regional  
858 liquid water sea or the regional thickening of a global ocean beneath the SPT, which may be a  
859 result of locally enhanced tidal heating and would itself contribute to the enhanced tidal  
860 heating<sup>27,54,55</sup>. The SPT is cryovolcanically active, as revealed by the plume of water vapor and  
861 icy particles emanating from the parallel “tiger stripe” fractures in the centre of the SPT<sup>24</sup>.  
862 Cassini Imaging Science Subsystem (ISS) images reveal the SPT to be bound by a quasi-  
863 rectangular set of tectonic structures with straight sides and angular intersections<sup>24</sup>. These border  
864 structures occur near the edges of the topographic depression containing the SPT<sup>24</sup>, located either  
865 at or just above the topographic step leading from the SPT up to the surrounding surface<sup>25</sup> (Fig.  
866 3c). The SPT is characterized by low topography<sup>25,56</sup> that is largely isostatically compensated at  
867 long wavelengths<sup>57</sup>, which is best explained by the presence of a dense subsurface ocean<sup>57,58</sup>.  
868 Depressions in other areas of Enceladus<sup>25</sup> have been explained as a result of the thermal  
869 annealing of the pore space due to the presence of local thermal anomalies beneath these regions  
870 in the past<sup>59</sup>. Some contribution to the SPT depression from a reduction of the pore space seems  
871 probable given the high observed heat flow. However, the large apparent depth of compensation

872 of the SPT indicated by the long-wavelength gravity and topography suggests that the effect of a  
873 deeper ocean dominates<sup>57</sup>.

874 Although there are notable large-scale morphological and geodynamic similarities  
875 between the PKT and the SPT, there are many differences between these provinces as well. The  
876 thermal anomaly in the SPT is a result of tidal, rather than radiogenic, heating. Multiple  
877 mechanisms have been proposed to explain the high heat flux in the SPT, including viscous  
878 heating in the ice shell<sup>55</sup> and shear heating along fractures<sup>60</sup>. Each of these mechanisms  
879 ultimately relies on tidal energy from the gravitational interaction of Enceladus with Saturn.  
880 However, the expected steady-state rate of tidal heating for the present-day eccentricity<sup>61</sup> is not  
881 sufficient to maintain the observed heat flux within the SPT<sup>26,53</sup> or the inferred subsurface ocean  
882 beneath the region<sup>27</sup>. Recent results have revised the lower bounds on the heat flow downward<sup>52</sup>,  
883 but values remain above the expected steady-state tidal heating unless the dissipation within  
884 Saturn is higher than expected from theoretical considerations<sup>62</sup>. This discrepancy may be  
885 explained if the SPT today is in a transient state of high heatflow following an earlier high  
886 eccentricity phase during which the ocean formed<sup>27</sup>. This scenario implies a time-variable heat  
887 flux in which the SPT may be cooling today.

888 The lack of craters within the SPT<sup>24</sup> suggests an earlier episode of volcanic resurfacing,  
889 lithosphere recycling<sup>28,63</sup>, or viscous relaxation of the craters<sup>64</sup>. Each of these scenarios could  
890 have resulted in a regional thermal anomaly, followed by a period of cooling and contraction of  
891 the ice throughout the SPT. Globally, substantial lateral and temporal variations in the heat flux  
892 have been inferred on the basis of high local heat fluxes indicated by the relaxation of craters<sup>64</sup>  
893 and the flexural support of topography<sup>65</sup>. Structures similar in scale and morphology to the SPT

894 on the leading and trailing hemispheres suggest similar activity at those locations in the past<sup>66</sup>,  
895 further supporting spatial and temporal variability in the thermal state of Enceladus' ice shell.

896 The SPT border structures are each composed of a belt of closely spaced parallel ridges,  
897 surrounded by an inward (southward) facing scarp<sup>24,67</sup>. The ridge belts likely formed by  
898 compression<sup>24,25</sup>, though extensional deformation<sup>68</sup> or more complicated scenarios<sup>69</sup> may have  
899 played a role in the formation of the south-facing scarps. For the compressional interpretation, it  
900 has been proposed that the tectonics in the SPT was driven by regional thermal expansion<sup>70</sup>,  
901 which is similar in nature but opposite in sign to what is proposed here for the PKT. At some  
902 intersections, the border scarps are continuous with fracture belts extending northward from  
903 120°-angle triple junctions<sup>67</sup>, consistent with an extensional origin for the outer scarp. However,  
904 the folded terrains confined within the angular corners are indicative of compressional  
905 deformation<sup>24</sup>. Compressional folding is also observed in the interior of the SPT away from the  
906 border structures<sup>71</sup>, whereas tensile opening of the “tiger stripe” fractures is required to explain  
907 the observed volcanic venting<sup>72</sup>. Thus, both compressional and extensional tectonics have been  
908 active along the border structures and within the interior of the SPT.

909 Some structures observed within the SPT are to first order consistent with our model  
910 predictions for the PKT. The models predict the upper lithosphere within a cooling lithospheric  
911 cap to be in a state of compression due to its coupling with the contracting lower lithosphere,  
912 whereas the cap would be surrounded by a belt in which extensional stresses pervade the entire  
913 lithosphere (Figure 4, Extended Data Figs 6–7). This stress pattern predicts broad compressional  
914 deformation of the upper lithosphere within the SPT and lithosphere-scale normal faulting at the  
915 margins. However, we emphasize that simple thermal expansion and contraction alone cannot

916 explain the extensive tectonism within the SPT. The extensive tectonic modification and  
917 resulting large strains may indicate an earlier period of mobile-lithosphere tectonics<sup>28,63</sup>.

918 Enceladus is much smaller than the Moon (radii of 252 and 1738 km, respectively).  
919 Although the SPT is much smaller than the PKT in physical size (~300 km versus ~2000 km),  
920 they are similar in angular size (Fig. 3). Thus, the geometric arguments for the formation of the  
921 quasi-rectangular PKT border structures due to the intersection of tectonic structures at 120°  
922 angles on a spherical surface may have relevance to the SPT as well.

923 Thus, we suggest that broadly similar geodynamic processes may have been at work in  
924 the PKT and the SPT. Both regions are characterized by strong thermal anomalies, enhanced  
925 volcanic activity, and low topography. The quasi-rectangular structures surrounding both  
926 provinces are consistent with the expected shapes of sets of tectonic structures intersecting at  
927 120°-angle triple junctions. However, the specific evolutionary paths of the provinces were  
928 likely substantially different. The source of heat, temporal variations in heat flux, and rheology  
929 of the lithosphere would have been substantially different in each case. Our current  
930 understanding of the formation and evolution of both structures is incomplete. Nevertheless, both  
931 provinces highlight the important effect that regional thermal anomalies can have on the regional  
932 volcanic and tectonic evolution of diverse planetary bodies.

933

#### 934 **Methods references**

935 <sup>31</sup> Reed, G. B., Application of kinematical geodesy for determining short wave length  
936 components of the gravity field by satellite gradiometry. *Technical Report No. 201*,  
937 Department of Geodetic Science, The Ohio State University, Columbus, Ohio (1973).

938 <sup>32</sup> Wieczorek, M. A. and Phillips, R. J., Potential anomalies on a sphere: Applications to the  
939 thickness of the lunar crust. *J. Geophys. Res.* **103**, 1715–1724 (1998).

940 <sup>33</sup> Kiefer, W. S. et al., The density and porosity of lunar rocks. *Geophys. Res. Lett.* **39**,  
941 L07201, doi:10.1029/2012GL051319 (2012).

942 <sup>34</sup> Parmentier, E. M., Zhong, S., and Zuber, M. T., Gravitational differentiation due to initial  
943 chemical stratification: Origin of lunar asymmetry by the creep of dense KREEP? *Earth*  
944 *Planet. Sci. Lett.* **201**, 473–480 (2002).

945 <sup>35</sup> Hess, P. C. and Parmentier, E. M., A model for the thermal and chemical evolution of the  
946 Moon's interior: Implications for the onset of mare volcanism. *Earth Planet. Sci. Lett.*  
947 **134**, 501–514 (1995).

948 <sup>36</sup> Elkins-Tanton, L. T., Burgess, S., and Yin, Q.-Z., The lunar magma ocean: Reconciling  
949 the solidification process with lunar petrology and geochronology. *Earth Planet. Sci.*  
950 *Lett.* **304**, 326–336 (2011).

951 <sup>37</sup> Elkins-Tanton, L. T., Van Orman, J. A., Hager, B. H., and Grove, T. L., Re-examination  
952 of the lunar magma ocean cumulate overturn hypothesis: melting or mixing is required.  
953 *Earth Planet. Sci. Lett.* **196**, 239–249 (2002).

954 <sup>38</sup> DeHon, R. A., Maximum thickness of materials in the western mare basins. *Lunar*  
955 *Planet. Sci. Conf.* **9**, 229–231 (1978).

956 <sup>39</sup> Blakely, Richard J., *Potential Theory in Gravity and Magnetic Applications*. (Cambridge  
957 University Press, Cambridge, 1995).

958 <sup>40</sup> Hiesinger, H., Jaumann, R., Neukum, G., and Head, J. W., Ages of mare basalts on the  
959 lunar nearside. *J. Geophys. Res.* **105**, 29,239–29,275, doi:10.1029/2000JE001244 (2000).

960 41 Hiesinger, H. et al., Ages and stratigraphy of mare basalts in Oceanus Procellarum, Mare  
961 Nubium, Mare Cognitum, and Mare Insularum. *J. Geophys. Res.* **108**, 5065,  
962 doi:10.1029/2002JE001985 (2003).

963 42 Pritchard, M. E. and Stevenson, D. J., Thermal aspects of a lunar origin by giant impact,  
964 in *Origin of the Earth and Moon*, edited by R.M. Canup and K. Righter (University of  
965 Arizona Press, Tucson, Ariz., 2000), pp. 179–196.

966 43 Goins, N. R., Dainty, A. M., and Toksoz, M. N., Structure of the lunar crust at highland  
967 site Apollo station 16. *Geophys. Res. Lett.* **8**, 29–32 (1981).

968 44 Presley, M. A. and Christensen, P. R., Thermal conductivity measurements of particulate  
969 materials: 4. Effect of bulk density for granular particles. *J. Geophys. Res.* **115**, E07003,  
970 doi:10.1029/2009JE003482 (2010).

971 45 Besserer, J. et al., Theoretical and observational constraints on lunar mega-regolith  
972 thickness. *Lunar Planet. Sci.* **44**, abstract 2463 (2013).

973 46 Turcotte, D. L. and Schubert, G., *Geodynamics*, 2<sup>nd</sup> ed. (Cambridge University Press,  
974 Cambridge, 2001).

975 47 Karato, S. and Wu, P., Rheology of the upper mantle: A synthesis. *Science* **260**, 771–778  
976 (1993).

977 48 Buck, W.R., Modes of continental lithospheric extension. *J. Geophys. Res.* **96**, 20,161–  
978 20,178 (1991).

979 49 McGovern, P. J. et al., Impact-generated loading and lithospheric stress gradients at lunar  
980 impact basins: Implications for maria emplacement scenarios. *Lunar Planet. Sci.* **44**,  
981 abstract 3055 (2013).

982 <sup>50</sup> Wilson, L. and Head, J. W., Ascent and eruption of basaltic magma on the Earth and  
983 Moon. *J. Geophys. Res.* **86**, 2971–3001 (1981).

984 <sup>51</sup> Lachenbruch, A. H., Mechanics of thermal contraction cracks and ice-wedge polygons in  
985 permafrost. *Geol. Soc. Amer. Spec. Paper* **70**, 1–66 (1962).

986 <sup>52</sup> Spencer, J. R. et al., Enceladus heat flow from high spatial resolution thermal emission  
987 observations. *EPSC Abstracts* **8**, EPSC2013-2840-2011 (2013).

988 <sup>53</sup> Spencer, J. R. et al., Cassini encounters Enceladus: Background and the discovery of a  
989 south polar hot spot. *Science* **311**, 1401–1405 (2006).

990 <sup>54</sup> Roberts, J. H. and Nimmo, F., Near-surface heating on Enceladus and the south polar  
991 thermal anomaly. *Geophys. Res. Lett.* **35**, L09201, doi:10.1029/2008GL033725 (2008).

992 <sup>55</sup> Tobie, G., Cadek, O., and Sotin, C., Solid tidal friction above a liquid water reservoir as  
993 the origin of the south pole hotspot on Enceladus. *Icarus* **196**, 642–652 (2008).

994 <sup>56</sup> Thomas, P. C. et al., Shapes of the Saturnian icy satellites and their significance. *Icarus*  
995 **190**, 573–584 (2007).

996 <sup>57</sup> Iess, L. et al., The gravity field and interior structure of Enceladus. *Science* **344**, 78–80  
997 (2014).

998 <sup>58</sup> Collins, G. C. and Goodman, J. C., Enceladus' south polar sea. *Icarus* **189**, 72–82 (2007).

999 <sup>59</sup> Besserer, J., Nimmo, F., Roberts, J. H., and Pappalardo, R. T., Convection-driven  
1000 compaction as a possible origin of Enceladus's long wavelength topography. *J. Geophys.*  
1001 *Res.* **118**, 908–915, doi:10.1002/jgre.20079 (2013).

1002 <sup>60</sup> Nimmo, F., Spencer, J. R., Pappalardo, R. T., and Mullen, M. E., Shear heating as the  
1003 origin of the plumes and heat flux on Enceladus. *Nature* **447**, 289–291 (2007).

1004 <sup>61</sup> Meyer, J. and Wisdom, J., Tidal heating in Enceladus. *Icarus* **188**, 535–539 (2007).



1005 <sup>62</sup> Lainey, V. et al., Strong tidal dissipation in Saturn and constraints on Enceladus' thermal  
1006 state from astrometry. *Astrophys. J.* **752**, 14 (2012).

1007 <sup>63</sup> Barr, A. C., Mobile lid convection beneath Enceladus' south polar terrain. *J. Geophys.*  
1008 *Res.* **113**, E07009, doi:10.1029/2008JE003114 (2008).

1009 <sup>64</sup> Bland, M. T., Singer, K. N., McKinnon, W. B., and Schenk, P. M., Enceladus' extreme  
1010 heat flux as revealed by its relaxed craters. *Geophys. Res. Lett.* **39**, L17204,  
1011 doi:10.1029/2012GL052736 (2012).

1012 <sup>65</sup> Giese, B. et al., Enceladus: An estimate of heat flux and lithospheric thickness from  
1013 flexurally supported topography. *Geophys. Res. Lett.* **35**, L24204,  
1014 doi:10.1029/2008GL036149 (2008).

1015 <sup>66</sup> Crow-Willard, E. and Pappalardo, R. T., Global geological mapping of Enceladus. *EPSC*  
1016 *Abstracts* **6**, EPSC-DPS2011-2635-2011 (2011).

1017 <sup>67</sup> Spencer, J. R. et al., Enceladus: An active cryovolcanic satellite, in *Saturn from Cassini-*  
1018 *Huygens*, edited by M. K. Dougherty, L. W. Esposito, and S. M. Krimigis (Springer, New  
1019 York), 683-724, doi:10.1007/1978-1001-4020-9217-1006-1021 (2009).

1020 <sup>68</sup> Walker, C. C., Bassis, J. N., and Liemohn, M. W., On the application of simple rift basin  
1021 models to the south polar region of Enceladus. *J. Geophys. Res.* **117**, E07003,  
1022 doi:10.01029/2012JE004084 (2012).

1023 <sup>69</sup> Yin, A. and Pappalardo, R. T., Left-slip faulting along the tiger stripe fractures:  
1024 Implications for the tectonic evolution of the south polar terrain, Enceladus. *Lunar.*  
1025 *Planet. Sci.* **44**, abstract 1145 (2013).

1026 <sup>70</sup> Gioia, G., Chakraborty, P., Marshak, S., and Kieffer, S., Unified model of tectonics and  
1027 heat transport in a frigid Enceladus. *Proc. Nat'l. Acad. Sci.* **104**, 13,578–513,581 (2007).

1028 <sup>71</sup> Barr, A. C. and Preuss, L. J., On the origin of the south polar folds on Enceladus. *Icarus*  
1029 **208**, 499–503 (2010).

1030 <sup>72</sup> Hurford, T. A. et al., Eruptions arising from tidally controlled periodic openings of rifts  
1031 on Enceladus. *Nature* **447**, 292–294 (2007).

1032

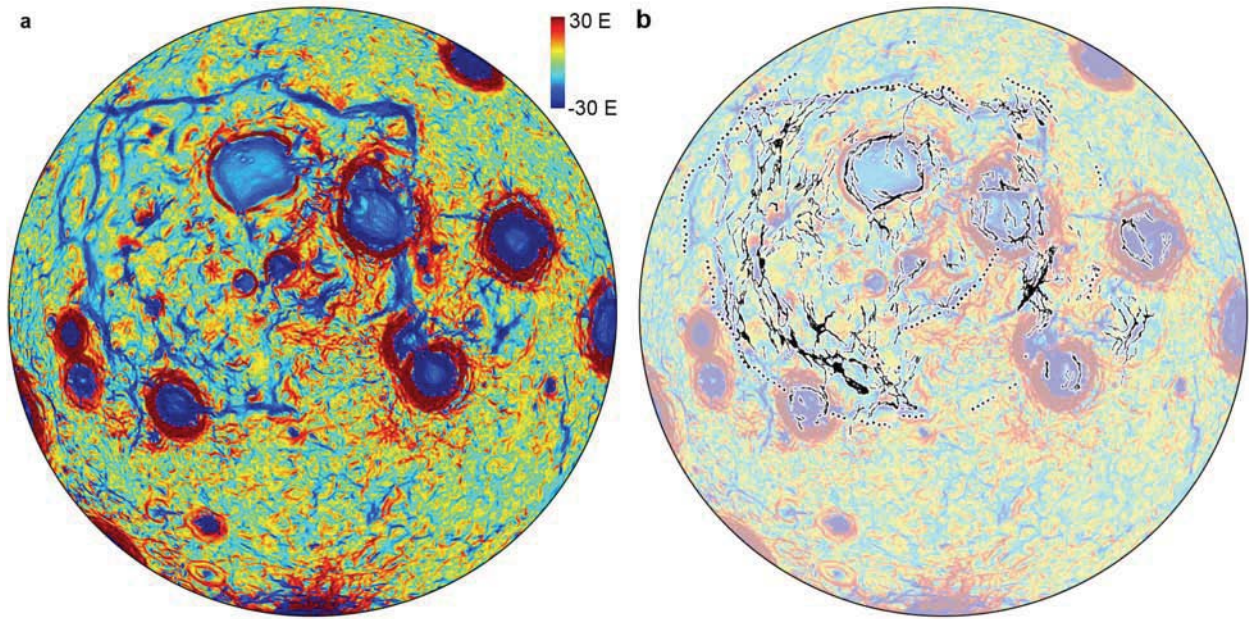
1033

1033 **Extended Data Table 1. Extension and strain across two border anomalies**

Filter	$\rho_M$ (kg/m <sup>3</sup> )	Anomaly 1		Anomaly 2	
		extension	strain	extension	strain
isostatic	3220	15 km	0.11	13 km	0.08
equal amplitude	3220	12 km	0.09	10 km	0.07
isostatic	3500	11 km	0.09	10 km	0.06
equal amplitude	3500	11 km	0.08	9 km	0.06
mare-crust only	3220	10 km	0.07	8 km	0.05
crust-mantle only	3220	16 km	0.12	18 km	0.12

1034

1035



1035

1036 **Extended Data Figure 1. Comparison of the GRAIL gravity gradients with proposed**

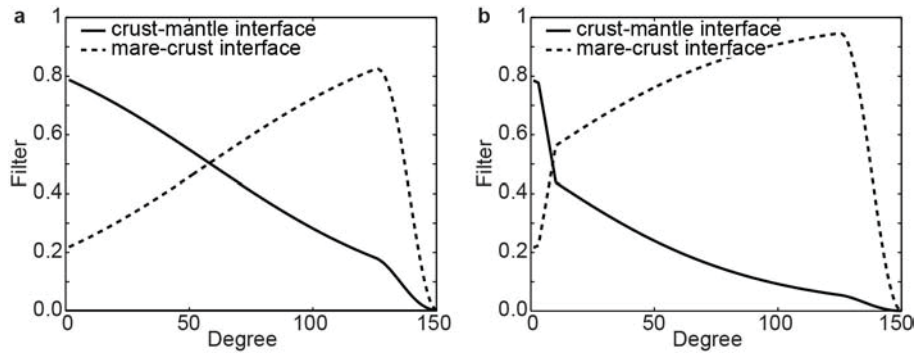
1037 **Procellarum basin ring structures. a, Bouguer gravity gradients (Eötvös) in a Lambert**

1038 azimuthal equal-area projection of the nearside of the Moon. **b, Muted gravity gradients overlaid**

1039 with mapped mare shorelines and scarps (dots) and wrinkle ridges (lines) (modified from Figure

1040 1 of *Whitaker*<sup>5</sup>).

1041



1041

1042 **Extended Data Figure 2. Filters applied during the crustal thickness modelling.** Filters

1043 were applied during the calculation of the relief along the crust-mantle interface (solid) and

1044 mare-crust interface (dashed) for cases in which the relief along the two interfaces was either **a**,

1045 isostatic prior to mare loading or **b**, equal and opposite in amplitude. The filter in **b** imposes the

1046 isostatic condition from degrees 1 to 3, with a linear transition to the equal amplitude filter from

1047 degrees 3 to 10. Both filters apply a cosine taper from degrees 125 to 150. The mare-crust filter

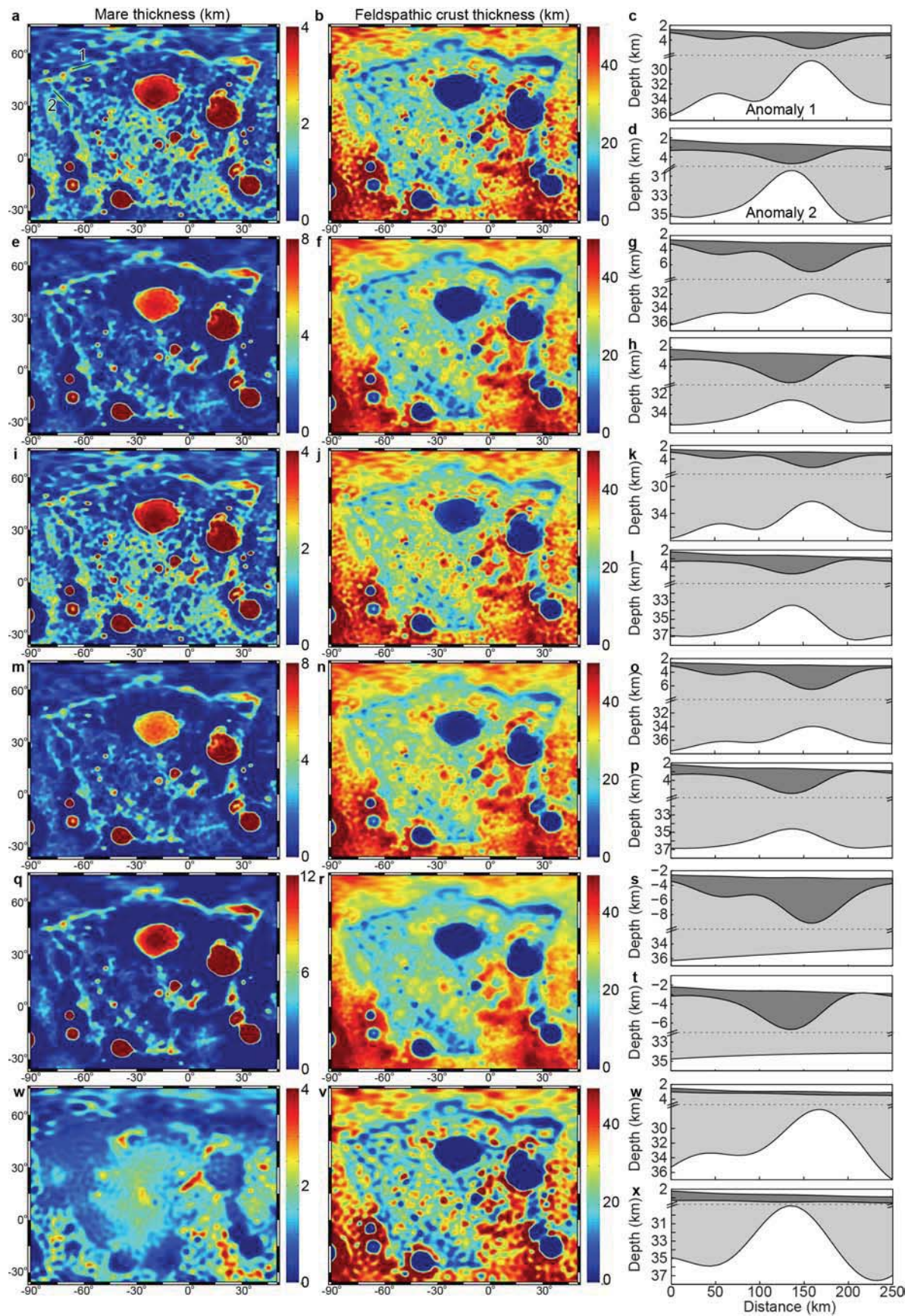
1048 is shown for illustration purposes only. In practice, the relief along the mare-crust interface was

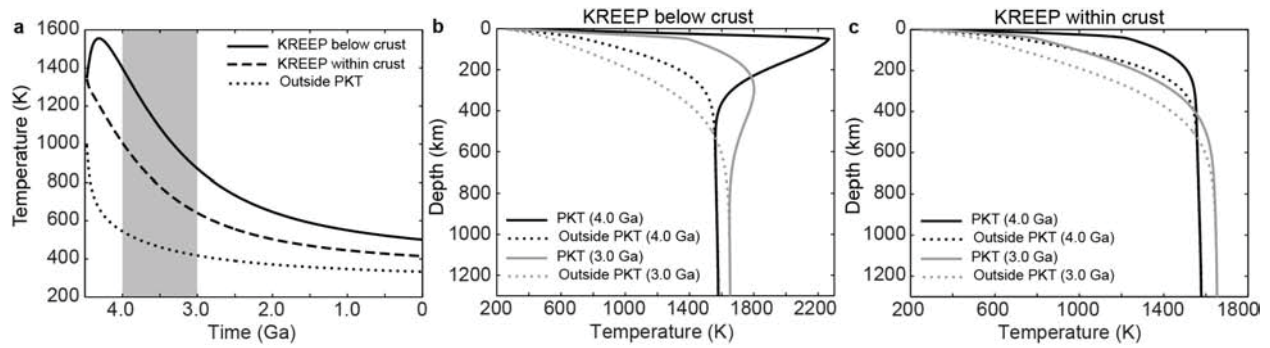
1049 calculated using the residual Bouguer anomaly after the calculation of the crust-mantle interface

1050 relief (equivalent to using the filter shown with the original Bouguer gravity).

1051

1051 **Extended Data Figure 3. (next page) Predicted thicknesses of the crust and maria and**  
1052 **average cross-sections across two of the anomalies.** Predicted thickness of the maria (left) and  
1053 underlying feldspathic crust (middle), and cross-sections of the modeled structure of anomaly 1  
1054 (right, top) and anomaly 2 (right, bottom) showing the variation in the thickness of the mare  
1055 (dark gray) and feldspathic crust (light gray). Models are for the cases of **a-d**, isostatic relief  
1056 along the two interfaces prior to mare infilling with a mantle density of  $3220 \text{ kg/m}^3$ , **e-h**, equal-  
1057 amplitude relief along the two interfaces with a mantle density of  $3220 \text{ kg/m}^3$ , **i-l**, isostatic relief  
1058 along the two interfaces prior to mare infilling with a mantle density of  $3500 \text{ kg/m}^3$ , **m-p**, equal-  
1059 amplitude relief along the two interfaces with a mantle density of  $3500 \text{ kg/m}^3$ , **q-t**, all gravity  
1060 anomalies at degrees  $>10$  ascribed to relief on the mare-crust interface, and **u-x**, all gravity  
1061 anomalies at degrees  $>10$  ascribed to relief on the crust-mantle interface.



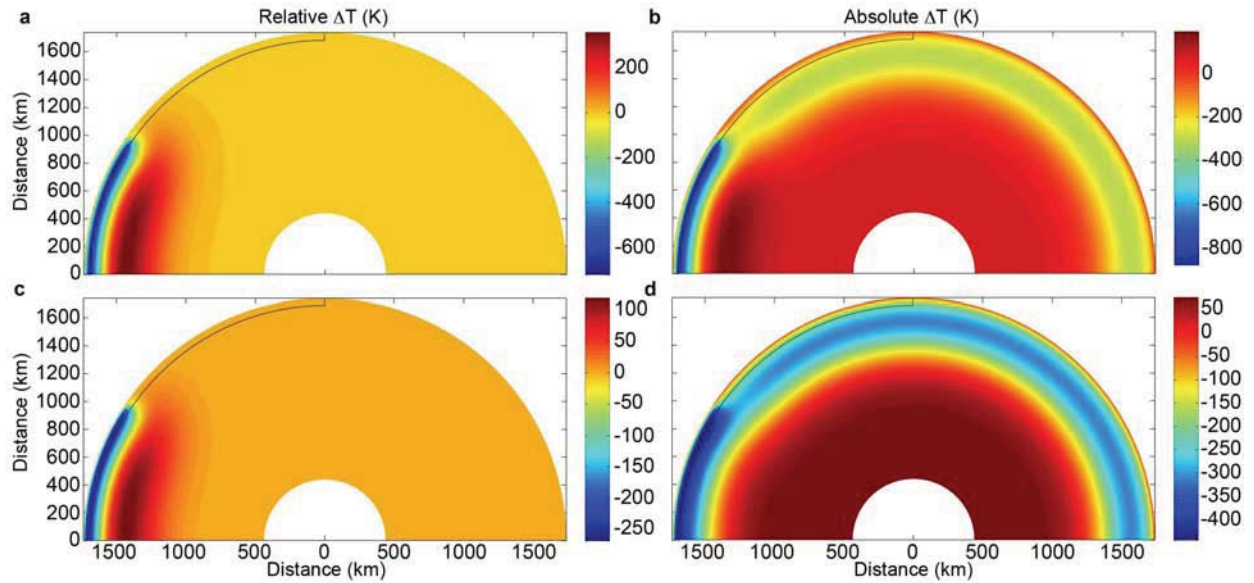


1063

1064 **Extended Data Figure 4. Temperature evolution at a depth of 25 km.** Temperatures are  
 1065 shown for **a**, KREEP-rich material concentrated at the base of the crust and **b**, KREEP-rich  
 1066 material distributed throughout the crust. The temperature at the base of the crust outside the  
 1067 PKT is shown for comparison. The period between 4.0 and 3.0 Ga that is the focus of the stress  
 1068 modeling is indicated by the shaded box.

1069





1069

1070 **Extended Data Figure 5. Predicted changes in temperature relative to areas outside the**

1071 **PKT and absolute temperature change between 4.0 and 3.0 Ga.** Results are shown for cases

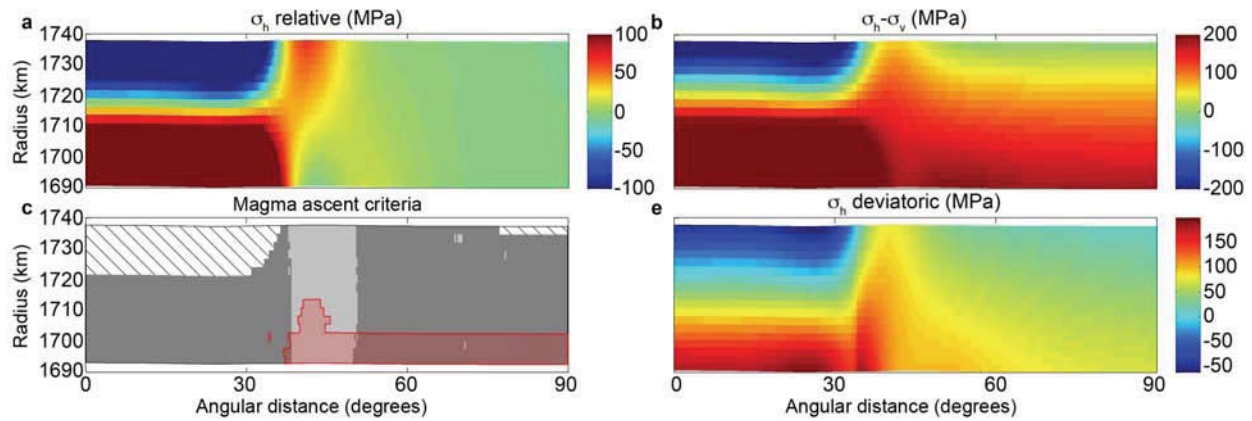
1072 with **a,b**, KREEP concentrated below the crust and **c,d**, KREEP distributed throughout the crust.

1073 The PKT is centred on the pole at the left side of the panels. The region shown in Extended Data

1074 Figs 6-7 (encompassing  $90^\circ$  of arc extending radially outward from the centre of the PKT and

1075 downward to a depth of 50 km) is outlined in black.

1076



1076

1077 **Extended Data Figure 6. Predicted lithospheric stresses and magma ascent for the case of**

1078 **10 km of KREEP at the base of the crust.** Cross-sections show **a**, the in-plane horizontal

1079 stresses (radial to the centre of the PKT, the far-field stress profile was subtracted to calculate the

1080 relative stress), **b**, the difference between the in-plane horizontal stress and the vertical stress, **c**,

1081 the magma ascent criteria, and **d**, the deviatoric stress. The magma ascent criteria reveals

1082 portions of the crust in which the horizontal stresses are tensile relative to the vertical stresses to

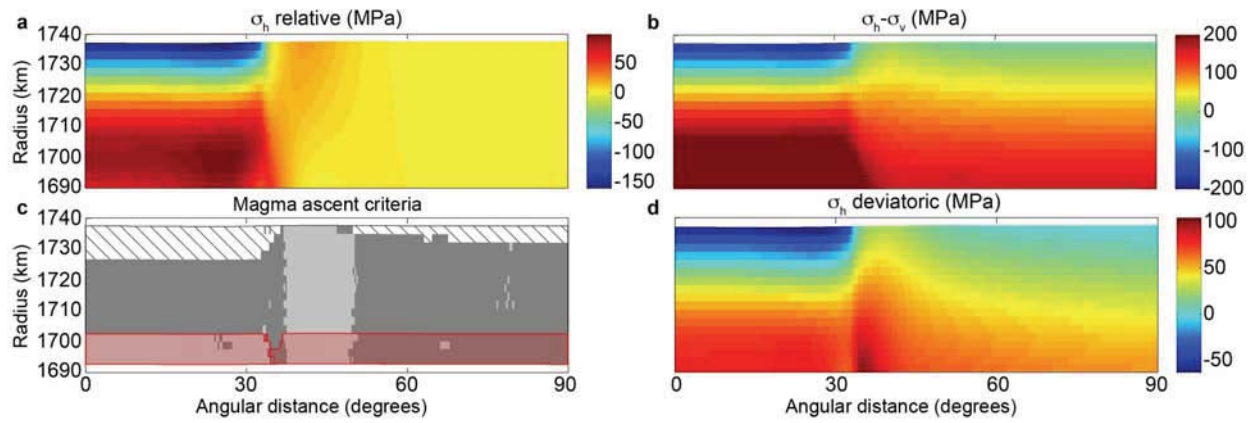
1083 permit the formation of vertical dikes (dark gray), where the vertical stress gradient is more

1084 favorable to magma ascent than the lithosphere far from the PKT (light grey), where magma will

1085 rise unassisted by other factors such as pressurized magma chambers (red), and where none of

1086 the criteria are satisfied (diagonal lines).

1087



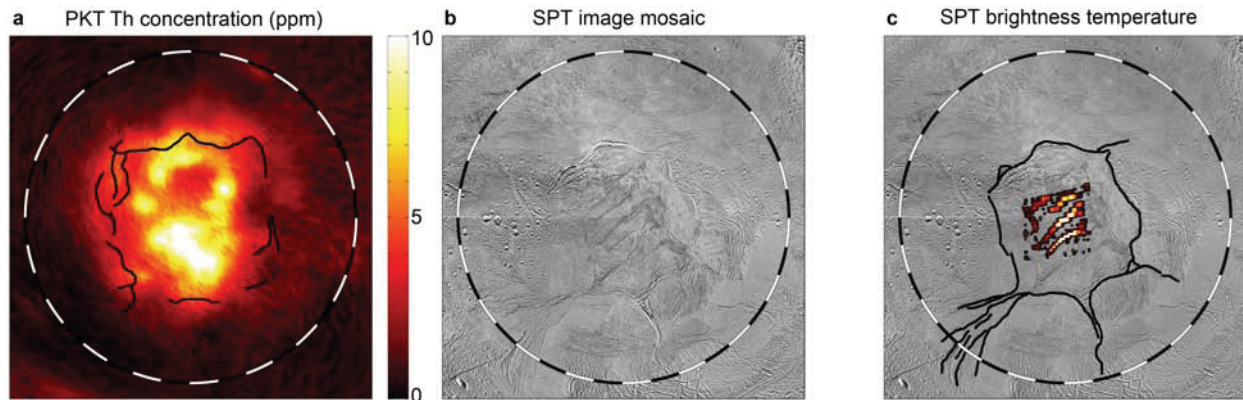
1087

1088 **Extended Data Figure 7. Predicted lithospheric stresses and magma ascent for the case of**

1089 **10 km of KREEP basalt distributed uniformly through a 40-km-thick crust. All panels are**

1090 **as in Extended Data Fig. 6.**

1091



1091  
 1092 **Extended Data Figure 8. Additional comparisons of Procellarum KREEP terrane to the**  
 1093 **Enceladus south polar terrain. a,** The PKT is characterized high heat flow as a result of the  
 1094 enhanced abundances of radioactive elements<sup>3</sup> (represented by the concentration of thorium<sup>4</sup>). **b,**  
 1095 The border structures of the SPT as revealed by Cassini ISS images<sup>24</sup> also trace a quasi-  
 1096 rectangular pattern enclosing a region of **c,** elevated brightness temperatures and enhanced heat  
 1097 flow<sup>26</sup>. All maps are in a simple polar projection. In all panels, the circle corresponds to an  
 1098 angular diameter of 180° of surface arc, divided into 10° increments.